

# Hyper-excitability and hyper-plasticity disrupt cerebellar signal transfer in the *IB2* KO mouse model of autism

Teresa Soda<sup>1,2\*\*</sup>, Lisa Mapelli<sup>1\*\*</sup>, Francesca Locatelli<sup>1</sup>, Laura Botta<sup>3</sup>, Mitchell Goldfarb<sup>4</sup>,  
Francesca Prestori<sup>1\*</sup>, Egidio D'Angelo<sup>1,5\*</sup>

<sup>1</sup> Dept of Brain and Behavioral Sciences, University of Pavia, Pavia, Italy

<sup>2</sup> Museo Storico della Fisica e Centro Studi e Ricerche Enrico Fermi, Rome, Italy

<sup>3</sup> Dept of Biology and Biotechnology "L. Spallanzani", University of Pavia, Pavia, Italy

<sup>4</sup> Dept of Biological Sciences, Hunter College, New York, USA

<sup>5</sup> Brain Connectivity Center, C. Mondino National Neurological Institute, Pavia, Italy

\* co-last authors

\*\* co-first authors

**Acknowledgments.** This project has received funding from: the European Union's Horizon 2020 Framework Programme for Research and Innovation under Grant Agreement No. 720270 (Human Brain Project SGA1); European Union grant Human Brain Project (HBP-604102); Fermi grant CNL to ED; Blue-Sky Research grant of the University of Pavia (BSR77992) to LM.

**Author contribution.** TS performed the bulk of electrophysiological experiments and data analysis, LM performed the whole set of imaging experiments and data analysis, FL performed part of the electrophysiological experiments, LB performed mice genotyping, MG provided the mice and contributed to paper discussion, FP performed the initial experiments and data analysis, ED LM and FP wrote the paper and ED coordinated the work.

**Running Title:** cerebellar alterations in autism

**Key words:** autism, cerebellum, excitatory/inhibitory balance, hyper-plasticity, NMDA receptor

## Abstract

Autism spectrum disorders (ASD) are pervasive neurodevelopmental conditions that often involve mutations affecting synaptic mechanisms. Recently, the involvement of cerebellum in ASD has been suggested but the underlying functional alterations remained obscure. We investigated single-neuron and microcircuit properties in *IB2* KO mice, which present a cerebellar phenotype associated with ASD. Granule cells showed a larger NMDA receptor-mediated current and enhanced intrinsic excitability raising the excitatory/inhibitory balance. Furthermore, the spatial organization of granular layer responses to mossy fibers shifted from a *Mexican hat* to *stovepipe hat* profile, with stronger excitation in the core and weaker inhibition in the surround. Finally, the size and extension of long-term synaptic plasticity was remarkably increased. These results show for the first time that hyper-excitability and hyper-plasticity disrupt signal transfer in the granular layer of *IB2* KO mice supporting cerebellar involvement in the pathogenesis of ASD.

## Introduction

Autism Spectrum Disorders (ASDs) are pervasive developmental disorders characterized by impairment in social communication and social interaction and by the presence of repetitive behaviors and/or restricted interests. ASDs cover a spectrum of different clinical conditions ranging from severely hypofunctional to hyperfunctional, and show abnormalities in different brain regions. Although most attention has been given so far to the cerebral cortex, increasing evidence implicates also the cerebellum (Amaral, 2011; Betancur, 2011; Ellegood et al., 2015). Cerebellar lesions often cause autistic-like symptoms (Hampson and Blatt, 2015) and perinatal cerebellar injuries are the greatest non-genetic risk factor for ASD (Bolduc and Limperopoulos, 2009; Limperopoulos et al., 2009; Bolduc et al., 2011; Wang et al., 2014; Mosconi et al., 2015). Moreover, cerebellar alterations are found in several syndromic forms of ASD, like Phelan-McDermid, Fragile X, Tuberous Sclerosis and Rett syndrome [for recent reviews, see (Courchesne and Allen, 1997; Schmahmann, 2004; Allen, 2006; Ito, 2008; D'Angelo and Casali, 2013; Broussard, 2014; Hampson and Blatt, 2015; Mosconi et al., 2015; Zeidán-Chuliá et al., 2016)]. This raises a main question: are there any alterations of cerebellar microcircuit functions in ASD?

ASDs are often associated with mutations in genes coding for synaptic proteins (Qiu et al., 2012; Banerjee et al., 2014; De Rubeis and Buxbaum, 2015; Kim et al., 2016) bringing about neurotransmission abnormalities (Curatolo et al., 2014; Ellegood et al., 2015; Kloth et al., 2015; Mercer et al., 2016; Sztainberg and Zoghbi, 2016; Tsai, 2016; Tu et al., 2017). The consequent microcircuit alterations have mainly been analyzed in the neocortex revealing that: (i) hyper-reactivity to stimulation, accompanied by altered neuronal excitability and synaptic plasticity, was related to increased glutamatergic transmission (Rinaldi et al., 2007; Markram et al., 2008; Rinaldi et al., 2008c; Markram and Markram, 2010); (ii) dysregulation of the excitatory/inhibitory (E/I) balance was related to various alterations at excitatory and inhibitory synapses (Rubenstein and Merzenich, 2003; Gogolla et al., 2009; Uzunova et al., 2015); (iii) altered modular organization of microcircuits (Casanova, 2003, 2006; Hutsler and Casanova, 2016) was related to reduced lateral inhibition, bringing about changes in the spatial organization of neuronal activation and synaptic plasticity. In particular, center-surround (C/S) structures were proposed to change from a "Mexican hat" to a "stovepipe hat" profile (Casanova, 2006).

A key role in synaptic and microcircuit dysregulation has been suggested by NMDA receptor hyperfunction and NMDA receptor antagonists have been recently reported to mitigate ASD symptoms in *Mef2c* mice models of Rett syndrome (Tu et al., 2017). Important for the present case, NMDA receptor-mediated currents were increased in cerebellar granule cells of the IB2 (Islet Brain-2) KO mouse, a model of the Phelan-McDermid syndrome (Giza et al., 2010). IB2 (MAPK8IP2) is a scaffolding protein enriched in the PSD, probably regulating signal transduction by protein kinase cascades, that operates inside the NMDA receptor interactome (Yasuda et al., 1999). Since NMDA receptor expression in granule cells is the highest among cerebellar neurons (Monaghan and Cotman, 1985) and has a profound impact on synaptic excitation and plasticity (D'Angelo et al., 1995; Armano et al., 2000; Sola et al., 2004; D'Errico et al., 2009), IB2 KO mice actually provide an ideal model to investigate cerebellar microcircuit alterations in ASD. In the cerebellar granular layer, granule cells receive excitatory synapses from mossy fibers and are inhibited by Golgi cells. The synaptic interaction between these neurons forms the granular layer microcircuit which, once activated by incoming spike bursts, generates responses organized in C/S

88 (Mapelli and D'Angelo, 2007; Gandolfi et al., 2014). Here we show that the granular layer of IB2  
89 KO mice is characterized by hyper-excitability and hyper-plasticity, which raise the E/I balance  
90 disrupting C/S structures and signal transfer at the input stage of cerebellum. The implications of  
91 these cerebellar microcircuit alterations for ASD pathogenesis are discussed.

92

93

94

95

96

97

98

99

100

101

102

103

104

105

106

107

108

109

110

111

112

113

114

115

116

117

118

119

120

121

122

123

124

125

126

127

128

129

130

131

## Methods

All procedures were conducted in accordance with European guidelines for the care and use of laboratory animals (Council Directive 2010/63/EU) and approved by the Ethical Committee of Italian Ministry of Health (637/2017-PR).

### *Genotyping and maintenance of IB2 KO mice*

Experiments were conducted on IB2<sup>+/+</sup> (WT) and IB2<sup>-/-</sup> (KO) mice obtained by crossing IB2<sup>+/-</sup> parents, since IB2 KO are poor breeders, possibly reflecting the social deficit associated with IB2 deletion (Giza et al., 2010). The genotyping was conducted through PCR using four primers to detect wild-type and null alleles as previously described (Giza et al., 2010).

### *Slice preparation and solutions*

The experiments reported in this paper have been conducted on 17-to 24-day-old (P0=day of birth) WT and IB2 KO mice. Mice were anesthetized with halothane (Sigma, St.Louis, MO) and killed by decapitation in order to remove the cerebellum for acute slice preparation according to a well-established technique (D'Angelo et al., 1995; Armano et al., 2000; Gall et al., 2005; Prestori et al., 2013; Nieuwenhuis et al., 2014). The vermis was isolated and fixed on the vibroslicer's stage (Leica VT1200S) with cyano-acrylic glue. Acute 220  $\mu$ m-thick slices were cut in the parasagittal plane in ice cold (2–3°C) Krebs solution containing (in mM): 120 NaCl, 2 KCl, 1.2 MgSO<sub>4</sub>, 26 NaHCO<sub>3</sub>, 1.2 KH<sub>2</sub>PO<sub>4</sub>, 2 CaCl<sub>2</sub>, and 11 glucose, equilibrated with 95% O<sub>2</sub>-5% CO<sub>2</sub> (pH 7.4). Slices were allowed to recover at room temperature for at least 1h, before being transferred to a recording chamber mounted on the stage of an upright microscope (Zeiss, Oberkochen, Germany). The slices were perfused with oxygenated Krebs's solution and maintained at 32°C with a Peltier feedback device (TC-324B, Warner Instrument Corp., Hamden, CT). For electrophysiological recordings, Krebs's solution was added with the GABA<sub>A</sub> receptor antagonist SR95531 (gabazine, 10  $\mu$ M; Sigma). In some experiments, Krebs's solution was Mg<sup>2+</sup>-free. Local perfusion with Krebs solution and 10  $\mu$ M SR95531 was commenced before seal formation and was maintained until end of recording. In a set of experiments the GABA<sub>A</sub> receptor antagonist SR95531 was omitted from the Krebs solution.

### *Electrophysiological recordings*

Whole-cell patch-clamp recordings were performed with Multiclamp 700B [-3dB; cutoff frequency (fc),10 kHz], sampled with Digidata 1440A interface, and analyzed off-line with pClamp10 software (Molecular Devices, CA, USA). Patch pipettes were pulled from borosilicate glass capillaries (Sutter Instruments, Novato, CA) and filled with different solutions depending on the specific experiments (see below). Mossy fiber stimulation was performed with a bipolar tungsten electrode (Clark Instruments, Pangbourne, UK) via a stimulus isolation unit. The stimulating electrode was placed over the central fiber bundle in the cerebellar lamina to stimulate

132 the mossy fibers, and 200  $\mu$ s step current pulses were applied at the frequency of 0.1-0.33 Hz (in  
133 specific experiments, paired-pulse stimulation at 20 ms inter-pulse was used). From a comparison  
134 with data reported in (Sharma and Vijayaraghavan, 2003; Giza et al., 2010; Sgritta et al., 2017), 1 or  
135 2 mossy fibers were stimulated per granule cell in the experiments used for quantal analysis. Long-  
136 term potentiation (LTP) induction was obtained by a continuous stimulation of 100 pulses at 100Hz  
137 at -50 mV (HFS), as reported previously (Armano et al., 2000; Gall et al., 2005; D'Errico et al.,  
138 2009; Prestori et al., 2013). Results are reported as mean  $\pm$  SEM and compared for their statistical  
139 significance by unpaired Student's test (unless otherwise stated; a difference was considered  
140 significant at  $p < 0.05$ ).

141 The stability of whole-cell recordings can be influenced by modification of series resistance  
142 ( $R_s$ ). To ensure that  $R_s$  remained stable during recordings, passive electrode-cell parameters were  
143 monitored throughout the experiments. The granule cell behaves like a lumped electrotonic  
144 compartment and can therefore be treated as a simple resistive - capacitive system, from which  
145 relevant parameters can be extracted by analyzing passive current relaxation induced by step  
146 voltage changes. In each recording, once in the whole-cell configuration, the current transients  
147 elicited by 10 mV hyperpolarizing pulses from the holding potential of -70 mV in voltage-clamp  
148 mode showed a biexponential relaxation, with a major component related to a somatodendritic  
149 charging (Prestori et al., 2008). According to previous reports (D'Angelo et al., 1995; Silver et al.,  
150 1996; D'Angelo et al., 1999), the major component was analyzed to extract basic parameters useful  
151 to evaluate the recordings conditions and to compare different cell groups. Membrane capacitance  
152 ( $C_m$ ) was measured from the capacitive charge (the area underlying current transients) and series  
153 resistance was calculated as  $R_s = \tau_{vc}/C_m$ . The membrane resistance ( $R_m$ ) was computed from the  
154 steady-state current flowing after termination of the transient. The 3-dB cut-off frequency of the  
155 electrode-cell system was calculated as  $f_{vc} = (2\pi \cdot \tau_{vc})^{-1}$ . The data are reported in Table 1. In the  
156 cells considered for analysis, these values did not significantly change after 30 minutes attesting  
157 recording stability. Cells showing variation of series resistance ( $R_s$ )  $>20\%$  were discarded from  
158 analysis.

### 159 160 *Granule cell excitability*

161 Patch pipettes had 7-9 M $\Omega$  resistance before seal formation with a filling solution containing  
162 (in mM): 126 potassium gluconate, 4 NaCl, 5 Hepes, 15 glucose, 1 MgSO<sub>4</sub>·7H<sub>2</sub>O, 0.1 BAPTA-free,  
163 0.05 BAPTA-Ca<sup>2+</sup>, 3 Mg<sup>2+</sup>-ATP, 0.1 Na<sup>+</sup>-GTP, pH 7.2 adjusted with KOH. The calcium buffer is  
164 estimated to maintain free calcium concentration around 100 nM. Just after obtaining the cell-  
165 attached configuration, electrode capacitance was carefully cancelled to allow for electronic  
166 compensation of pipette charging during subsequent current-clamp recordings. At the beginning of  
167 each recording, a series of depolarizing steps was applied in voltage-clamp to measure the total  
168 voltage-dependent current of the granule cell (see Fig. 1C). Leakage and capacitance were  
169 subtracted using a hyperpolarizing pulses delivered before the test pulse (P/4 protocol). After  
170 switching to current-clamp, intrinsic excitability was investigated (see Fig. 1B) by setting resting  
171 membrane potential at -80 mV and injecting 800-ms current steps (from - 4 to 22 pA in 2 pA  
172 increment). Membrane potential during current steps was estimated as the average value between  
173 600 and 800 ms. Action potential frequency was measured by dividing the number of spikes by step  
174 duration.

175

176 *Post-synaptic currents*

177 Patch pipettes had 5–8 M $\Omega$  resistance before seal formation with a filling solution  
178 containing the following (in mM): 81 Cs<sub>2</sub>SO<sub>4</sub>, 4 NaCl, 2 MgSO<sub>4</sub>, 1 QX-314 (lidocaine N-ethyl  
179 bromide), 0.1 BAPTA-free and 0.05 BAPTA-Ca<sup>2+</sup>, 15 glucose, 3 Mg<sup>2+</sup>-ATP, 0.1 Na<sup>+</sup>-GTP, and 15  
180 HEPES, pH adjusted to 7.2 with CsOH. The calcium buffer is estimated to maintain free calcium  
181 concentration around 100 nM. Synaptic currents elicited at 0.33 Hz were averaged and digitally  
182 filtered at 1.5 kHz off-line. IPSC and EPSC peak amplitude were taken at +10 and -70 mV to  
183 measure the GABA<sub>A</sub> and AMPA currents, respectively. In some experiments, NMDA current was  
184 directly measured at -70 mV in Mg<sup>2+</sup>-free solution in the presence of the AMPA receptor blocker,  
185 10  $\mu$ M NBQX (Sola et al., 2004). In LTP experiments, the acquisition program automatically  
186 alternated EPSC with background activity recordings (1 s and 9 s, respectively), from which  
187 mEPSCs were detected. After 10 min (control period), the recording was switched to current clamp  
188 (patch pipettes were filled with a K<sup>+</sup>-gluconate based solution) and high-frequency stimulation  
189 (HFS) was delivered to induce plasticity. Long-term synaptic efficacy changes were measured after  
190 20 min. After delivering HFS, voltage-clamp at -70 mV was reestablished and stimulation was  
191 restarted at the test frequency. EPSCs and mEPSCs were digitally filtered at 1.5 kHz and analyzed  
192 off-line with pClamp10 software (Molecular Devices, Sunnyvale, CA). For both EPSC and mEPSC  
193 peak amplitude was computed. mEPSC detection was performed automatically with Mini  
194 Analysis Program (Synaptosoft, Inc. Decatur, GA) when their amplitude was 5-7 time the baseline  
195 noise S.D. ( $0.88 \pm 0.03$ ;  $n=8$ ). These criteria and a further visual inspection of detected signals  
196 allowed us to reject noise artifacts.

197 In order to investigate the expression mechanism of long-term synaptic plasticity over a  
198 heterogeneous data set (Sola et al., 2004; Gall et al., 2005), a simplified version of quantal analysis  
199 was performed by measuring the mean (M) and standard deviation (S) of EPSC amplitude. EPSC  
200 changes, which do not strictly require that single synaptic connections are isolated, were obtained  
201 from M and S: the coefficient of variation,  $CV = S/M$ , the paired-pulse ratio,  $PPR = M_2/M_1$ , i.e. the  
202 ratio between the second and first EPSC amplitude in a doublet at 20 ms inter-pulse interval. The  
203 comparison between M and CV obtained before and after the induction of plasticity could be  
204 performed in the plot  $(CV_2/CVA_1)^{-2}$  vs.  $(M_2/M_1)$ . Assuming binomial statistics, this plot has the  
205 property that the unitary slope diagonal separates points caused by changes in quantum content ( $m$   
206 =  $np$ , with  $n$  being the number of releasing sites and  $p$  the release probability) from those caused by  
207 changes in quantum size ( $q$ ). The inequality leads to a topological representation of  
208 neurotransmission changes (see Fig.7) and has been extensively used to interpret the plasticity  
209 mechanism (Bekkers and Stevens, 1990; Malinow and Tsien, 1990; Sola et al., 2004; Rinaldi et al.,  
210 2008a; D'Errico et al., 2009; Sgritta et al., 2017). For an M increase:

- 211 (i) when  $(CV_2/CVA_1)^{-2} > (M_2/M_1)$  both  $n$  and  $p$  can increase,  
212 (ii) when  $(CV_2/CVA_1)^{-2} = (M_2/M_1)$  only  $n$  can increase,  
213 (iii) when  $(CV_2/CVA_1)^{-2} < (M_2/M_1)$  neither  $n$  nor  $p$  can increase implying an increase in  $q$ . A  
214 pure increase in  $q$  will lie on the axis when  $(CV_2/CVA_1)^{-2} = 1$ .

215  
216 *Voltage sensitive dye imaging (VSDi)*

217 The stock solution for VSDi contained the dye Di-4-ANEPPS (Molecular Probes, Eugene,  
218 OR) dissolved in a Krebs-based solution containing 50% ethanol (Sigma) and 5% Cremophor EL  
219 (Sigma). Slices for optical recordings were incubated for 30 minutes in oxygenated Krebs solution

220 added with 3% Di-4-ANEPPS stock solution and mixed with an equal volume of fetal bovine serum  
221 (Molecular Probes) to reach a final dye concentration of 2 mM (Vranesic et al., 1994). After  
222 incubation, the slices were rinsed with Krebs solution to wash out the dye that was not incorporated  
223 by the tissue, before being transferred to the recording chamber installed on an upright  
224 epifluorescence microscope (Slicescope, Scientifica Ltd, Uckfield, UK), equipped with a 20X  
225 objective (XLUMPlanFl 0.95 NA, water immersion; Olympus, Tokyo, Japan). The light generated  
226 by a halogen lamp (10V150W LM150, Moritex, Tokyo, Japan) was controlled by an electronic  
227 shutter (Newport corporation, Irvine, CA) and then passed through an excitation filter ( $\lambda = 535 \pm 20$   
228 nm), projected onto a dichroic mirror ( $\lambda = 565$  nm) and reflected toward the objective lens to  
229 illuminate the specimen. Fluorescence generated by the tissue was transmitted through an  
230 absorption filter ( $\lambda > 580$  nm) to the CCD camera (MICAM01, Scimedia, Brainvision, Tokyo,  
231 Japan). The whole imaging system was connected through an I/O interface (Brainvision) to a PC  
232 controlling illumination, stimulation and data acquisition. The final pixel size was  $4.5 \times 4.5 \mu\text{m}$  with  
233 20X objective. Full-frame image acquisition was performed at 0.5 kHz. Data were acquired and  
234 displayed by Brainvision software and signals were analyzed using custom-made routines written in  
235 MATLAB (Mathworks, Natick, MA). At the beginning of recordings, a calibration procedure was  
236 adopted to ensure homogeneity across experiments. The dynamic range of the CCD camera was  
237 calibrated by measuring background fluorescence and setting the average light intensity in the  
238 absence of stimulation to 50% of the saturation level. The background fluorescence was sampled  
239 for 50 ms before triggering electrical stimulation and was used to measure the initial fluorescence  
240 intensity ( $F_0$ ). The relative fluorescence change ( $\Delta F/F_0$ ) was then calculated for each time frame.  
241 The signal-to-noise ratio was improved by averaging 10 consecutive sweeps at the stimulus  
242 repetition frequency of 0.1 Hz.

243

#### 244 *VSDi data analysis*

245 Fluorescence data collected by Brainvision acquisition software were filtered using both a  
246 cubic filter (3x3) and a spatial filter (3x3) embedded in the software, and then exported and  
247 processed in Matlab. The resulting files were a series of matrices each representing a temporal  
248 frame of the acquired trace. Using appropriate Matlab routines written *ad hoc*, single matrices  
249 representing the peak value of granular layer responses to electrical stimulation were obtained.  
250 These maps containing the information on the signal peak amplitudes and their spatial origin were  
251 used for comparison of control condition and different treatments, as detailed below. Data were  
252 reported as mean  $\pm$  SEM. Statistical significance was assessed using unpaired Student's t test unless  
253 otherwise stated. For the analysis of the amount and spatial distribution of the NMDA receptor  
254 component of excitation in the cerebellar granular layer of WT and IB2 KO mice, responses to  
255 electrical stimulation of the mossy fibers were recorded in control and after perfusion of the NMDA  
256 receptor blocker APV (50  $\mu\text{M}$ ). The average map of APV effect on signal amplitudes was  
257 subtracted to the control map, to unveil the contribution of the NMDA receptors. The spatial  
258 distribution of the NMDA receptor-mediated depolarization was revealed by averaging each  
259 experimental map on the peak of NMDA receptor component in each case. Whenever spatial maps  
260 obtained from different experiments were averaged, the corresponding slices were aligned along the  
261 mossy fiber bundle. For the analysis of the excitatory/inhibitory (E/I) balance and spatial  
262 distribution of excitation and inhibition in the granular layer, similar experiments were carried out,  
263 recording the responses to MFs stimulation before and after the perfusion of the GABA<sub>A</sub> receptor

264 antagonist SR95531 (gabazine; 10  $\mu$ M). This approach allows to reconstruct a map of regions with  
265 prevailing excitation (E) compared to regions showing prevailing inhibition (I) (Mapelli and  
266 D'Angelo, 2007; Gandolfi et al., 2014). In this case, the E map was constructed on the control  
267 responses (where the response is available only in the regions where excitation prevails over  
268 inhibition), while the I map was constructed subtracting the maps after SR95531 perfusion to the  
269 control maps (unveiling the regions where, before SR95531 perfusion, excitation was prevented by  
270 inhibition). Both E and I maps were normalized to 1, and the E/I balance maps were obtained as (E-  
271 I)/E. The C/S organization of excitation and inhibition was evident averaging the E/I maps in each  
272 experiment on the peak of excitation in controls. For the analysis of the amount and spatial  
273 distribution of LTP and LTD in the granular layer, plasticity maps were obtained by comparing  
274 responses amplitudes before and after the plasticity induction through a HFS delivered to the mossy  
275 fiber bundle. The C/S spatial organization of LTP and LTD was unveiled by averaging each  
276 plasticity maps from different experiments on the peak of maximum LTP.

277

278

279

## Results

280

281

282

283

284

285

286

287

288

289

In the cerebellum granular layer, there are three main mechanisms controlling the E/I balance of granule cells (Nieus et al., 2014): granule cells intrinsic excitability, mossy fiber glutamatergic excitation, Golgi cell GABAergic inhibition (Mapelli et al., 2014) (Fig.1A). Here, these properties have been compared in turn between IB2 KO and WT mice. In patch-clamp whole-cell recordings in acute cerebellar slices, there were no significant differences in either series resistance ( $R_s$ ), membrane resistance ( $R_m$ ), or resting membrane potential between IB2 KO and WT cerebellar granule cells (Table 1).

**Table 1. Properties of whole-cell recordings in mice granule cells**

	WT (n = 70)	IB2 KO (n = 57)
$R_m$ (G $\Omega$ )	2.3 $\pm$ 0.1	2.9 $\pm$ 0.3
$C_m$ (pF)	3.6 $\pm$ 0.09	3.2 $\pm$ 0.09 **
$R_s$ (M $\Omega$ )	15.9 $\pm$ 0.9	16.9 $\pm$ 1.0
$f_{vc}$ (KHz)	3.8 $\pm$ 0.3	3.5 $\pm$ 0.2
$\tau_{vc}$ ( $\mu$ s)	54.1 $\pm$ 3.0	60.5 $\pm$ 7.2
$V_m$ (mV)	-52.1 $\pm$ 2.6 (n=12)	-54.5 $\pm$ 2.0 (n=12)

290

291

292

293

294

295

The data were obtained using K-gluconate intracellular solution and analyzing current transient elicited by 10 mV voltage-clamp steps delivered from the holding potential of -70 mV. The number of observations indicated and statistical significance is reported in comparison with IB2 KO granule cells. \*\*p<0.01, unpaired t test.

[Source\\_Table1](#)

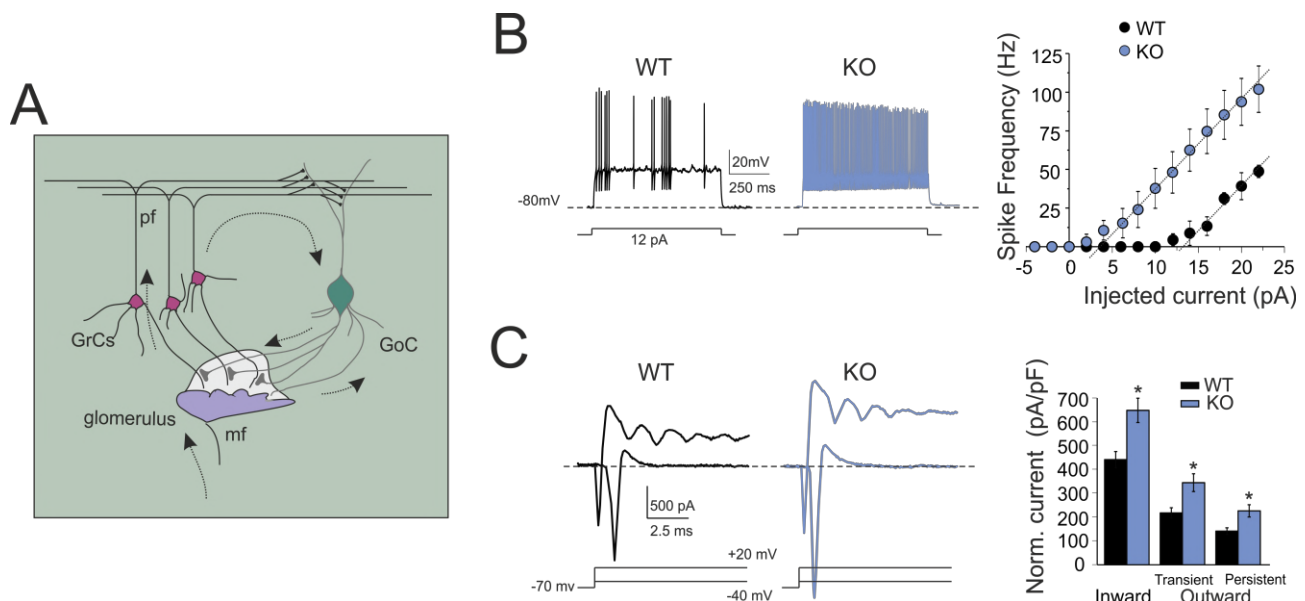
296

297 **Enhanced intrinsic excitability in IB2 KO granule cells**

298 In whole-cell current-clamp recordings, both WT and IB2 KO granule cells were silent at  
 299 rest and responded to current steps with fast repetitive spike discharges that increased their  
 300 frequency almost linearly with stimulus intensity (D'Angelo et al., 1995; Brickley et al., 1996;  
 301 D'Angelo et al., 1998; Rossi et al., 1998; Armano et al., 2000; Cathala et al., 2003; Prestori et al.,  
 302 2008) (Fig. 1B). However, IB2 KO granule cells showed higher discharge frequency compared to  
 303 WT granule cells both at low current injection [12 pA: WT =  $4.1 \pm 0.1$  Hz (n=6); IB2 KO =  $48.1 \pm$   
 304  $14.2$  Hz (n=8); p=0.017, unpaired *t*-test] and at high current injection [20 pA: WT =  $39.2 \pm 9.5$  Hz  
 305 (n=6); IB2 KO =  $93.7 \pm 16.0$  Hz (n=8); p=0.014, unpaired *t*-test], shifting the frequency-intensity  
 306 plot toward the left (Fig. 1B). It should be noted, as explained above and in Table 1, that the  
 307 enhanced intrinsic excitability in IB2 KO mice did not depend either on passive or resting  
 308 properties, which did not significantly differ in the two cell groups used in these experiments.

309 In the same experiments, whole-cell currents elicited by depolarizing voltage steps differed  
 310 in WT and IB2 KO granule cells (Fig. 1C). The “transient inward current” (corresponding to a fast  
 311 Na<sup>+</sup> current) (Magistretti et al., 2006) was significantly larger in IB2 KO compared to WT granule  
 312 cells. The “transient and persistent outward currents” (comprising A-type, delayed rectifier, and  
 313 calcium-dependent K<sup>+</sup> currents) (Bardoni and Belluzzi, 1994) were also significantly larger in IB2  
 314 KO compared to WT granule cells. Thus, the enhancement of intrinsic excitability in IB2 KO  
 315 granule cells was correlated with abnormal expression of voltage-dependent membrane currents.  
 316

317



318

319

320

321

322

323

324

325

326

327

328

329

**Figure 1. Granule cell excitable properties.**

(A) Schematic representation of cerebellar circuit. Mossy fibers (mf) contact granule cells (GrC) and Golgi cell (GoC) dendrites.

Axons of GrCs, the parallel fibers (pf), activate Golgi cells which inhibit GrCs through feedforward and feedback inhibitory loops.

(B) Granule cell electroresponsiveness. Voltage responses were elicited from -80 mV using step current injection. The plot shows the relationships between average spike frequency over 2 sec and the injected current intensity both for WT (n=6) and IB2 KO (n=8) granule cells. Linear fits (dashed lines): WT x-intercept 3 pA, slope  $7.8 \pm 1.6$  spike/pA (n=6); IB2 KO x-intercept 13 pA, slope  $6.4 \pm 0.5$  spike/pA (n=8). Data are reported as mean  $\pm$  SEM.

(C) Voltage-activated inward and outward currents in granule cells. Exemplar voltage-dependent currents evoked by depolarizing voltage steps from the holding potential of -70 mV were leak-subtracted. The histogram compares inward and outward current amplitudes measured at -40 mV and +20 mV in WT and IB2 KO mice. Data are reported as mean  $\pm$  SEM; \*p<0.05.

[Source\\_Figure1](#)



330

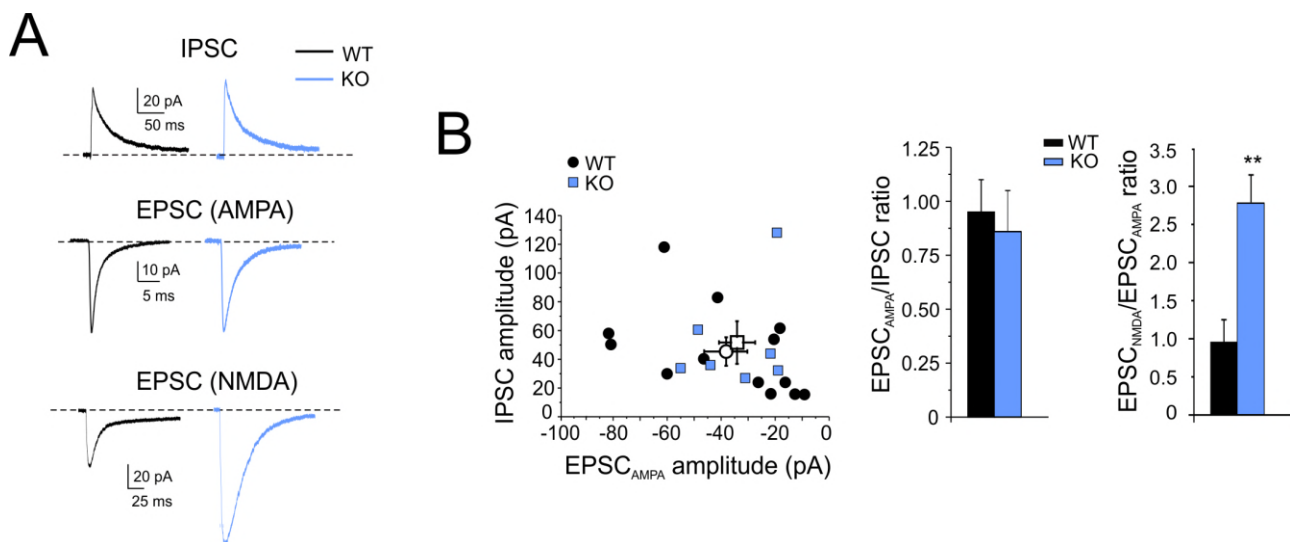
331 ***Similar AMPA and GABA<sub>A</sub> but increased NMDA receptor mediated currents at IB2 KO granule***  
332 ***cell synapses***

333 Mossy fiber stimulation is known to elicit EPSCs directly through mossy fiber activation  
334 and IPSCs indirectly through activation of Golgi cells (cfr. Fig.1A) (Cathala et al., 2003; Cesana et  
335 al., 2013; Nieuw et al., 2014). Postsynaptic currents were recorded from granule cells both at -70  
336 mV and +10 mV in order to isolate the excitatory (EPSC) from inhibitory (IPSC) component. This  
337 technique was reported previously (Mapelli et al., 2009; Nieuw et al., 2014). It should be noted that,  
338 at -70 mV, NMDA receptor-mediated currents are blocked by Mg<sup>2+</sup>, so that the EPSC is almost  
339 purely AMPA receptor-mediated. In the present experiments, the AMPA-EPSC peak (WT = -38.1  
340 ± 7.1 pA, n=13 vs. IB2 KO = -34.1 ± 5.7, n=7; p=0.66) and the GABA<sub>A</sub>-IPSC peak (WT = 45.4 ±  
341 8.4 pA, n=13 vs. IB2 KO = 51.7 ± 13.4, n=7; p=0.69) showed similar amplitude in WT and IB2 KO  
342 mice (Fig. 2A). Accordingly, no differences were observed in the AMPA-EPSC/GABA<sub>A</sub>-IPSC ratio  
343 in granule cells (WT = 0.95 ± 0.15, n=13 vs. IB2 KO = 0.86 ± 0.19, n=7; p=0.71; Fig. 2B).

344 In a different series of recordings, the NMDA EPSC was elicited in isolation at -70 mV in  
345 Mg<sup>2+</sup>-free solution in the presence of AMPA and GABA<sub>A</sub> receptor blockers (10 μM NBQX and 10  
346 μM SR95531, respectively; Fig. 2A). The NMDA-EPSC peak was enhanced in IB2 KO synapses  
347 (WT = -37.0 ± 5.1 pA, n=6 vs. IB2 KO = -95.3 ± 17.7, n=5; p=0.03) by 2.5 times. These results  
348 confirm the alteration in NMDA EPSC amplitude reported previously (Giza et al., 2010).

349 In aggregate, the similarity of the AMPA-EPSC and GABA<sub>A</sub>-IPSC, along with the large  
350 increase of the NMDA-EPSC, suggest that the excitatory/inhibitory (E/I) balance in IB2 KO mice  
351 will move in favor of excitation in conditions in which the NMDA channels are physiologically  
352 unblocked by depolarization.

353



354

355 **Figure 2. Evoked excitatory and inhibitory currents in granule cells.**

356 (A) Synaptic currents in WT and IB2 KO granule cells. The EPSC<sub>AMPA</sub> and IPSC are recorded from the same cells at the holding  
357 potential of -70 mV (averaging of 100 consecutive traces) and at +10 mV (averaging 10 consecutive traces), respectively. The  
358 EPSC<sub>NMDA</sub> are recorded in different cells at -70 mV in Mg<sup>2+</sup>-free extracellular solution in presence of the AMPA receptor antagonist,  
359 10 μM NBQX (averaging of 30 consecutive traces).

360 (B) IPSC/EPSC ratios at mossy fiber– granule cell synapses in WT and IB2 KO mice. The plot shows the amplitude of EPSC<sub>AMPA</sub>  
361 and IPSC in the same cells for WT and IB2 KO mice (open symbols are mean ± SEM). The histogram compares the average  
362 EPSC<sub>AMPA</sub>/IPSC ratio and EPSC<sub>NMDA</sub>/EPSC<sub>AMPA</sub> ratio in WT and IB2 KO mice (mean ± SEM; \*\*p<0.01).

363 [Source\\_Figure2](#)

364

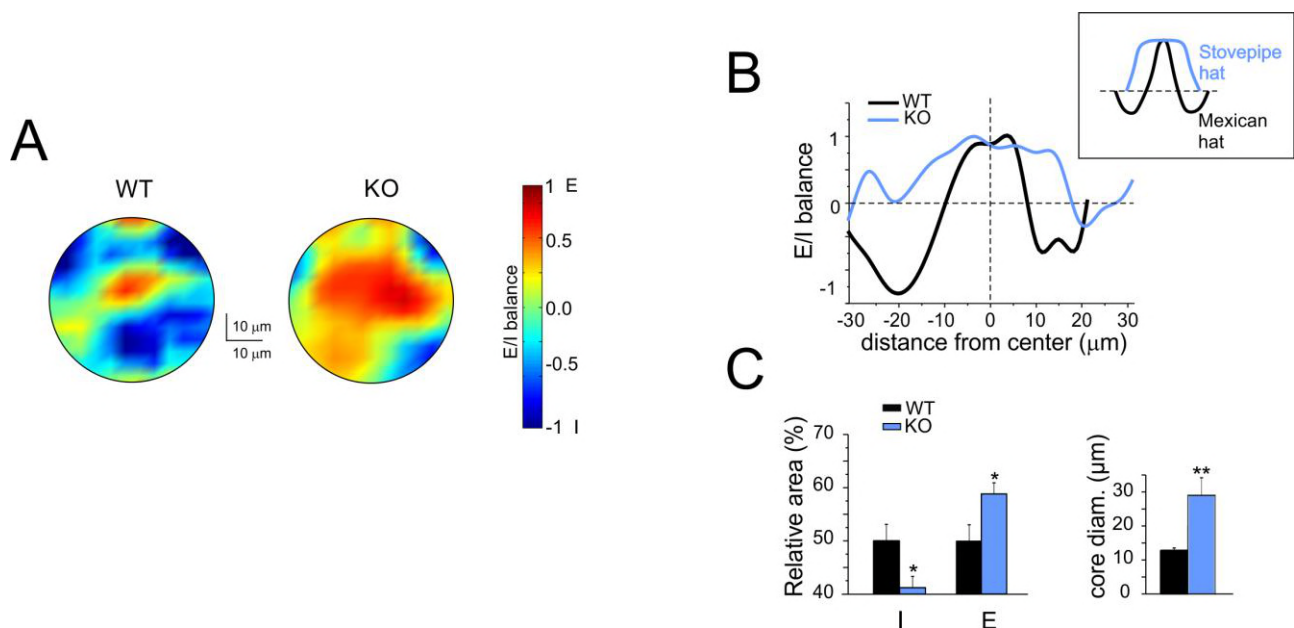
365

### 366 **Increased excitation in C/S structures of IB2 KO granular layer are driven by NMDA currents**

367 In order to obtain a physiological assessment of the E/I balance and of the NMDA current  
368 contribution, we used voltage-sensitive dye imaging (VSDi). VSDi allows to generate maps of  
369 electrical activity and to investigate the spatial distribution of granular layer responses following  
370 mossy fiber stimulation (Mapelli et al., 2010). In particular, VSDi, coupled with selective  
371 pharmacological blockade of synaptic receptors, can reveal the relative role of synaptic inhibition  
372 and of NMDA receptors (Gandolfi et al., 2015).

373 A first set of VSDi recordings was performed by subtracting control activity maps from  
374 those obtained after GABA<sub>A</sub> receptor blockade with 10  $\mu$ M SR95531 (Fig. 3; see Methods for  
375 details). In agreement with previous observations, the granular layer response to mossy fiber stimuli  
376 self-organized in center/surround (C/S) structures characterized by a "Mexican hat" profile, with an  
377 excitation core surrounded by inhibition (Mapelli and D'Angelo, 2007; Solinas et al., 2010;  
378 Gandolfi et al., 2014; Gandolfi et al., 2015) (Figs 3A,B). The C/S distribution was maintained in the  
379 IB2 KO granular layer but with striking differences. (i) Excitation was enhanced generating larger  
380 cores compared to WT (core diameter: WT =  $12.9 \pm 1.7 \mu$ m vs. IB2 KO =  $29.5 \pm 4.9 \mu$ m, n=5 for  
381 both; ; p=0.0106) (Fig. 3C). (ii) Inhibition was weaker in the surround (WT/KO ratio  $I_{WT/KO} = 2.83$   
382  $\pm 0.17$ , n=5). (iii) Granular layer areas showing excitation were consequently larger in IB2 KO than  
383 WT mice (WT =  $49.9 \pm 3.1\%$  vs. IB2 KO =  $58.8 \pm 2.1\%$ , n=5 for both; p=0.0468; Fig. 3C). As a  
384 result, the altered C/S organization in IB2 KO showed larger excitation cores with poor inhibitory  
385 surrounds, shifting from "Mexican hat" to the so-called "stovepipe hat" shape (see Fig. 3B).

386



387

388

### 389 **Figure 3. Excitatory/inhibitory balance and center/surround organization in the granular layer.**

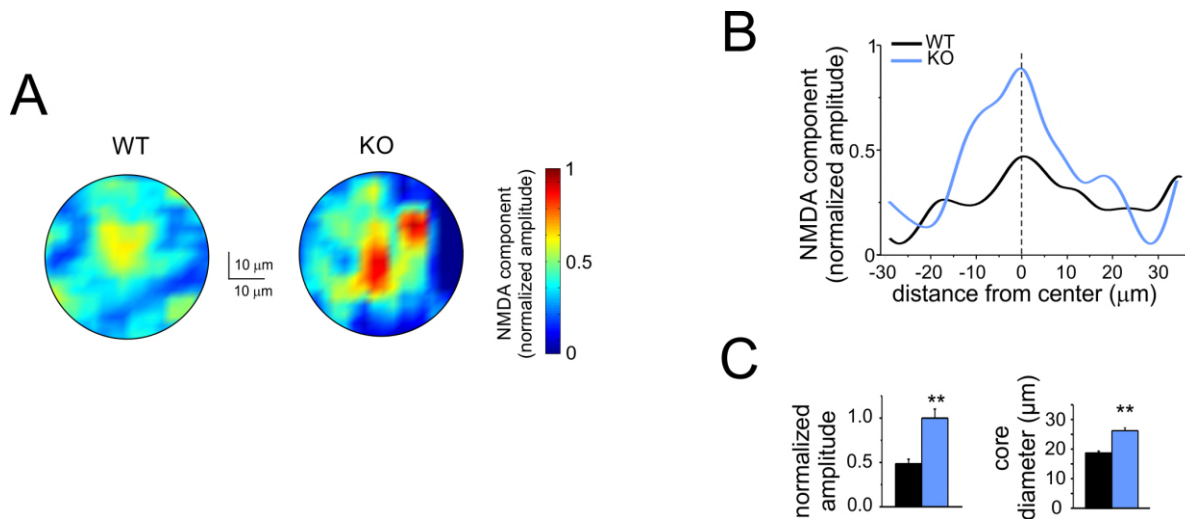
390 (A) VSDi normalized maps showing the spatial distribution of excitation and inhibition in WT and IB2 KO granular layer (average of  
391 5 recordings in both cases).

392 (B) The plot shows the E/I balance as a function of distance from the center for the maps shown in A. Note that in IB2 KO granular  
393 layer the excitation core is broader, while the inhibited surround is reduced, compared to WT. This tends to change the C/S from the  
394 typical Mexican hat in control to stovepipe hat shape in IB2 KO mice (cf. inset).

395 (C) The histograms show, in WT and IB2 KO mice, the average values of the inhibition or excitation areas and of core diameter  
396 (mean  $\pm$  SEM; \*p<0.05, \*\*p<0.01).

397 [Source\\_Figure3](#)

398 A second set of VSDi recordings was performed by subtracting control activity maps from  
399 those obtained after NMDA receptor blockade with 50  $\mu$ M APV (Fig. 4; see Methods for details).  
400 As expected from the increased NMDA receptor-mediated current reported in Fig. 2, the NMDA  
401 receptor-mediated component of the VSDi signal was larger in IB2 KO than WT granular layers  
402 (ratio KO/WT =  $2.16 \pm 0.29$ ,  $n=5$  for both). The maps showing the spatial organization of the  
403 NMDA receptor contribution to the excitatory response were similar to the C/S organization shown  
404 in Fig.3, with peaks of NMDA receptor contribution in cores with a diameter of  $26.1 \pm 1.7 \mu$ m in  
405 IB2 KO vs.  $18.9 \pm 1.6 \mu$ m in WT;  $n=5$  for both;  $p=0.015$  (Figs. 4A,B). Interestingly, since during  
406 VSDi membrane potential remains unclamped allowing voltage-dependent NMDA channel unblock  
407 during depolarization, these maps provide information about the non-linear contribution of NMDA  
408 currents. This result supported the hypothesis that the enhanced NMDA receptor-mediated  
409 transmission revealed in Fig. 2 was indeed a key player in determining the C/S and E/I alteration in  
410 IB2 KO granular layer.  
411  
412



413

414 **Figure 4. NMDA receptor-dependent component of granular layer excitation.**

415 (A) VSDi normalized maps showing the spatial distribution of the NMDA component of excitation in WT and IB2 KO granular layer  
416 (average of 5 recordings in both cases).

417 (B) The plot shows the NMDA component as a function of distance from the center for the maps shown in A. Note that in IB2 KO  
418 granular layer the NMDA component of excitation is larger and more extended compared to WT.

419 (C) The histograms show, in WT and IB2 KO mice, the average values of the NMDA component normalized amplitude and of core  
420 diameter (mean  $\pm$  SEM; \*\* $p<0.01$ ).

421 [Source\\_Figure4](#)

422

423

### 424 **Enhanced long-term potentiation at the IB2 KO mossy fiber-granule cell relay**

425 Mossy fiber-granule cell LTP is NMDA receptor-dependent through the synaptic control of  
426 postsynaptic intracellular calcium elevation (D'Angelo et al., 1999; Maffei et al., 2003; Gall et al.,  
427 2005; D'Errico et al., 2009). The impact of elevated NMDA receptor-dependent neurotransmission  
428 on LTP induction in IB2 KO mice was evaluated using a continuous high-frequency stimulation  
429 train (HFS; Fig. 5A) delivered from the holding potential of -50 mV in current-clamp (Gall et al.,  
430 2005; D'Errico et al., 2009). During HFS, IB2 KO generated more spikes than WT granule cells  
431 (WT =  $23.5 \pm 5.3$ ,  $n=12$  vs. IB2 KO =  $54.2 \pm 11.4$ ,  $n=9$ ;  $p=0.015$ ; Figs. 5A,B), in line with the

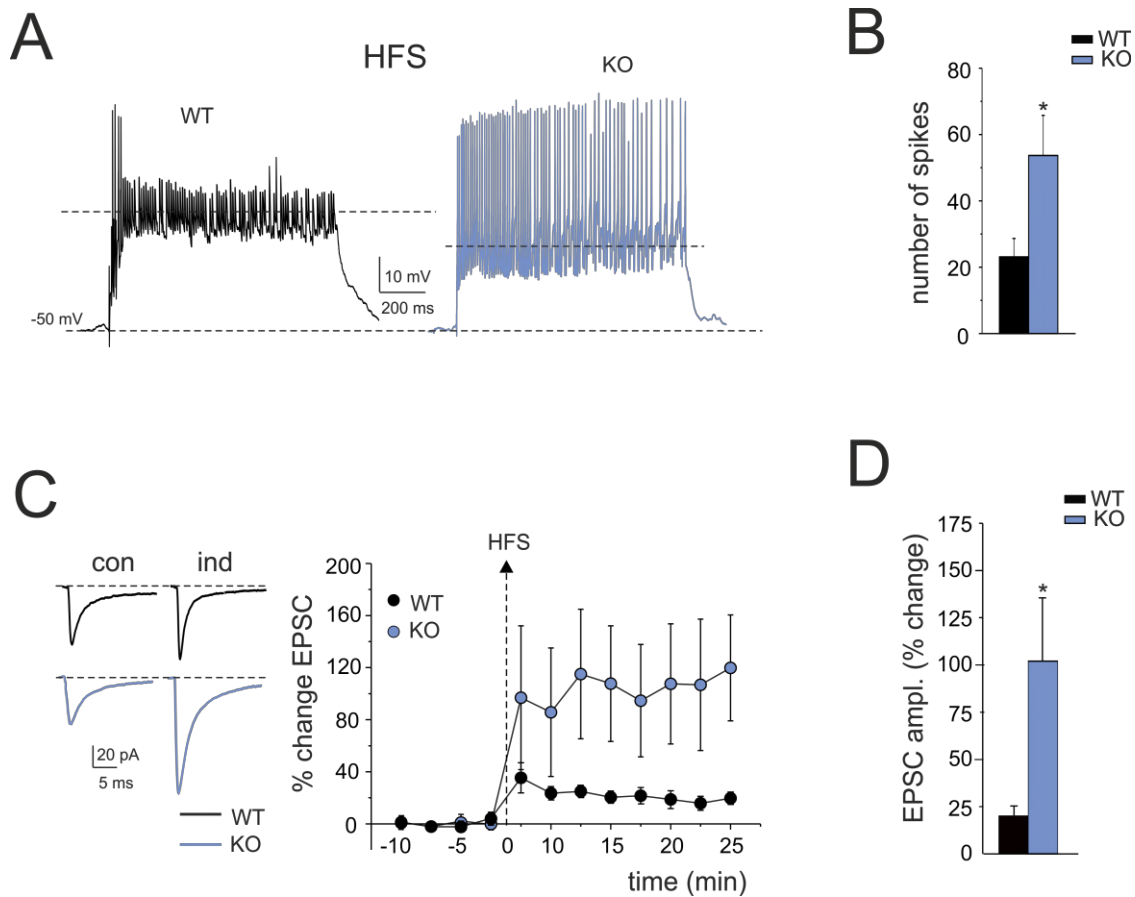
432 enhancement in NMDA currents (D'Angelo et al., 2005) and in intrinsic firing reported above (cf.  
433 Figs 1 and 2). After HFS, the changes were evaluated over at least 25 min after HFS.

434 The AMPA EPSC increased both in WT and IB2 KO mice and remained potentiated  
435 throughout the recordings (Fig. 5C). The increase in amplitude of AMPA-EPSCs was ~5-fold larger  
436 in IB2 KO than WT mice (WT =  $20.4 \pm 4.2\%$ , n=12 vs. IB2 KO =  $102.4 \pm 34.9\%$ , n=9; p=0.047;  
437 Fig. 5D).

438 Intrinsic excitability increased more in WT than in IB2 KO mice (Fig. 6A,B). The current  
439 needed to generate spikes (current threshold) decreased significantly compared to control in WT  
440 granule cells ( $-42.8 \pm 7.7\%$ , n=6; p=0.0055) but not in IB2 KO granule cells ( $-8.6 \pm 14.4\%$ , n=8;  
441 p=0.07; Fig. 6B). Moreover, the increase in spike frequency was less pronounced in IB2 KO than  
442 WT granule cells (WT =  $102.6 \pm 19.3\%$ , n=6 vs. IB2 KO =  $21.1 \pm 8.7\%$ , n=8; p=0.032; Fig. 6B). A  
443 possible explanation of this effect could be that granule cell intrinsic excitability was already  
444 increased in IB2 KO granule cells (cf. Fig.1B), such that the level of IB2 KO granule cell  
445 excitability in control was similar to that in WT granule cells after potentiation (Fig. 6B).

446 As a further control, we monitored the apparent granule cell input resistance (Fig. 6C,D) by  
447 measuring the response to small current steps (causing about 10 mV potential changes) either below  
448 -70 mV ( $R_{in-low}$ ) or above -70 mV ( $R_{in-high}$ ) (Armano et al., 2000). After HFS,  $R_{in-high}$  rapidly  
449 increased in both WT and IB2 KO mice, following a similar time course and remained potentiated  
450 throughout the recordings (at least 20 min after HFS; average time courses are shown in Fig. 6D).  
451 At 20 min after HFS,  $R_{in-high}$  increase was  $67.8 \pm 16.5\%$  (n=8) (p=0.0014) in WT and  $46.9 \pm 9.0\%$   
452 (n=10) in IB2 KO mice (p=0.00012). This change was likely to contribute to the increased intrinsic  
453 excitability in both WT and IB2 KO. It should be noted that  $R_{in-low}$  remained unchanged in both  
454 WT and IB2 KO, providing an internal control for recording stability (Fig. 6C,D).

455



456

457

458 **Figure 5. LTP of mossy fiber-granule cell EPSCs.**

459 (A) Granule cell synaptic responsiveness. Voltage responses were elicited from -50 mV during 1sec-100Hz synaptic stimulation

460 (HFS) used for plasticity induction. Note stronger spike generation in IB2 KO than WT.

461 (B) The histogram shows the average number of spikes during HFS in WT and IB2 KO mice. Data are reported as mean  $\pm$  SEM;

462 \* $p$ <0.05.

463 (C) LTP of EPSC<sub>AMPA</sub> in WT and IB2 KO granule cells (average of 100 tracings in both cases) recorded in control and 20 min after

464 HFS. Note that, after HFS stimulation, the EPSC<sub>AMPA</sub> increase was larger in IB2 KO than WT. The LTP plot shows the average time

465 course of EPSC<sub>AMPA</sub> amplitude changes in WT (n=12) and IB2 KO (n=9) granule cells. Data are reported as mean  $\pm$  SEM; \* $p$ <0.05).

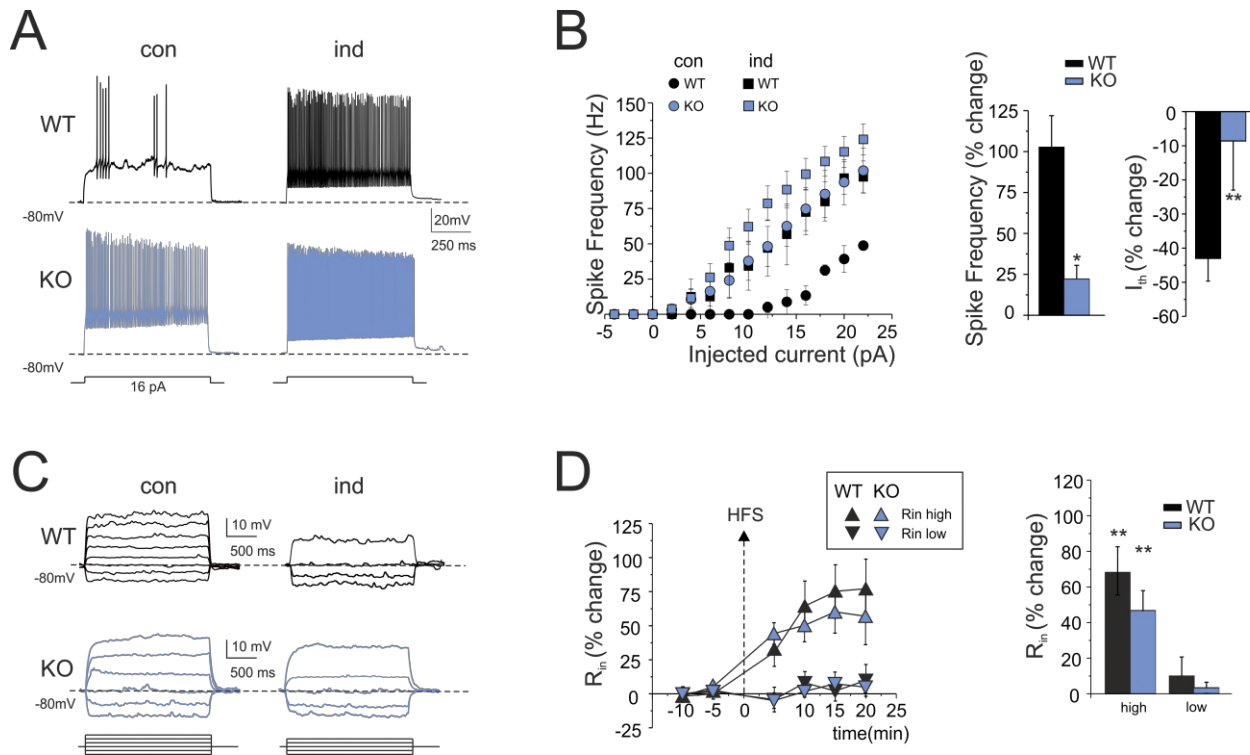
466 (D) The histogram shows the average EPSC<sub>AMPA</sub> LTP following HFS in WT and IB2 KO mice. Data are reported as mean  $\pm$  SEM;

467 \* $p$ <0.05.

468 [Source\\_Figure5](#)

469

470



471

472

473

474

475

476

477

478

479

480

481

482

483

484

485

486

487

488

489

490

491

492

493

494

495

496

497

498

499

500

501

**Figure 6. Long-term enhancement in granule cells intrinsic excitability.**

(A) Voltage responses to current injection in WT and IB2 KO granule cells recorded in control and 20 min after HFS. Note that HFS enhances spike generation both in WT and IB2 KO granule cells.

(B) Spike frequency is plotted as a function of current injection in control conditions and after HFS both in WT and IB2 KO mice. Note that, after HFS, spike frequency increases more in WT than in IB2 KO mice. The histograms compare the average spike frequency and threshold current ( $I_{th}$ ) changes in WT and IB2 KO mice. Data are reported as mean  $\pm$  SEM; \* $p < 0.05$ , \*\* $p < 0.01$ .

(C) Subthreshold voltage responses to current injection in WT and IB2 KO granule cells recorded in control and 20 min after HFS. Note that the voltage-response in the high-potential region is enhanced both in WT and IB2 KO granule cells.

(D) The plot shows the average time course of input resistance ( $R_{in}$ ) changes after HFS stimulation in two subthreshold membrane potential regions,  $< -70$  mV ( $R_{in-low}$ ) and  $> -70$  mV ( $R_{in-high}$ ). After HFS, in both WT and IB2 KO granule cells,  $R_{in-high}$  but not  $R_{in-low}$  increased. The histogram shows the average  $R_{in}$  changes for WT and IB2 KO mice. Data are reported as mean  $\pm$  SEM; \*\* $p < 0.01$ .

[Source\\_Figure6](#)

### **Different mechanisms of LTP expression in IB2 KO granule cells**

LTP expression was first assessed by analyzing changes in EPSC amplitude, variability (CV), and paired-pulse ratio (PPR) (Fig. 7A). The paired-pulse ratio (PPR) of EPSCs is generally considered to reflect changes in the probability of transmitter release in a pair of stimuli (Zucker and Regehr, 2002), while the coefficient of variation (CV) of EPSCs is a readout of presynaptic variability of quantal transmitter release upon repeated stimulation normalized by the mean (Malinow and Tsien, 1990; Manabe et al., 1993). In the recordings used for PPR and CV analysis, after HFS, the EPSCs showed a significant increase in WT ( $18.2 \pm 3.4$ ;  $n=8$ ;  $p=0.012$ ) and IB2 KO mice ( $106.8 \pm 51.8\%$ ;  $n=5$ ;  $p=0.05$ ), while PPR (interstimulus interval 20 ms) showed a significant reduction in WT ( $-19.6 \pm 9.3\%$ ;  $n=8$ ;  $p=0.033$ ) but not in IB2 KO ( $-6.7 \pm 3.3\%$ ;  $n=5$ ;  $p=0.1$ ). Interestingly, CV significantly decreased in both WT and IB2 KO (WT =  $-28.3 \pm 6.7$ ,  $n=12$ ;  $p=0.002$ ; IB2 KO =  $-30.0 \pm 8.0$ ,  $n=9$ ;  $p=0.012$ ). The CV decrease suggested that neurotransmitter release was increased not just in WT (Sola et al., 2004) but also in IB2 KO mice, although with some difference (see below).

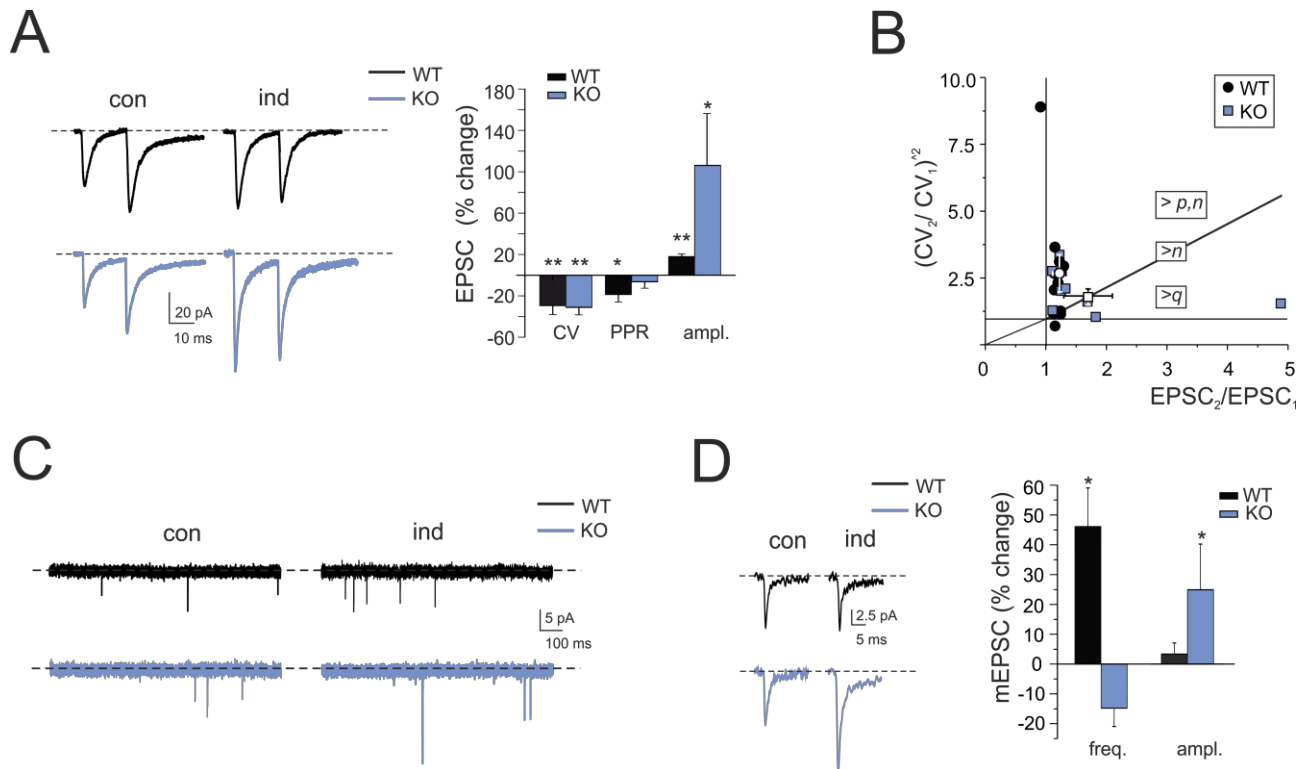
The CV and PPR analysis cannot stand alone in determining the changes that could affect the neurotransmission process (Yang and Calakos, 2013). A further way to assess whether EPSC

502 changes depend on the number of releasing sites ( $n$ ), release probability ( $p$ ) or quantum size ( $q$ ) is to  
503 plot  $(CV_2/CV_1)^{-2}$  versus  $(M_2/M_1)$  (Bekkers and Stevens, 1990; Malinow and Tsien, 1990) (Fig. 7B).  
504 The WT experimental data points were distributed homogeneously in the quadrant corresponding to  
505  $p/n$  increase, with no point falling in the regions of a pure  $n$  or  $q$  change. Conversely, the IB2 KO  
506 experimental dataset was heterogeneously distributed over regions of  $p$ ,  $n$  or  $q$  increase. These data  
507 distributions suggested that multiple presynaptic and postsynaptic mechanisms contributed to  
508 determine LTP at IB2 KO mossy fiber-granule cell synapses.

509 A second experimental approach to quantal analysis is to examine miniature postsynaptic  
510 currents (mEPSCs) before and after LTP induction (Fig. 7C,D) (Kullmann and Nicoll, 1992; Wyllie  
511 et al., 1994; Malgaroli et al., 1995). This method is especially useful at multi-quantal release  
512 synapses like here (Sola et al., 2004; Saviane and Silver, 2006) and can allow to distinguish  
513 between an increase in quantum content ( $p$  or  $n$ ) or quantum size ( $q$ ). Since here mEPSCs accounted  
514 for the whole spontaneous mossy fiber activity, in LTP experiments mEPSCs were recorded  
515 without TTX and were used to characterize the LTP expression mechanism (Sola et al., 2004).  
516 Moreover, in order to prevent mEPSC changes from being obscured by the contribution of non-  
517 potentiated synapses, we activated as many synapses as possible by raising stimulus intensity.  
518 Indeed, in these recordings, the EPSCs [ $(-59.0 \pm 11.0$  pA ( $n=4$ ) in WT and  $-55.0 \pm 14.9$  pA ( $n=4$ ) in  
519 IB2 KO mice] were about twice as large than those measured in Fig. 2 [(by comparison with single  
520 fiber EPSCs measured in similar recording conditions, this corresponded to activation of two to  
521 three mossy fibers (Sola et al., 2004)]. After HFS, the EPSCs increased (WT =  $19.0 \pm 2.0\%$ ,  $n=4$ ;  $p$   
522 = 0.02 vs. IB2 KO =  $93.6 \pm 49.7$ ,  $n=4$ ;  $p = 0.02$ ) confirming larger LTP induction in IB2 KO than  
523 WT mice (cf. Fig. 7A). In the same recordings, mEPSCs amplitude did not vary in WT granule cells  
524 ( $3.3 \pm 3.7\%$ ,  $n=4$ ;  $p = 0.4$ ) but showed significant increase in IB2 KO granule cells ( $28.9 \pm 5.66\%$ ,  
525  $n=4$ ;  $p = 0.016$ ). Conversely, mEPSC frequency showed a significant increase in WT granule cells  
526 ( $46.1 \pm 12.9\%$ ,  $n=4$ ;  $p = 0.016$ ) but did not show any significant changes in IB2 KO granule cells ( $-$   
527  $16.9 \pm 6.0\%$ ,  $n=4$ ;  $p = 0.11$ ). Therefore, mEPSC analysis indicated that, while WT granule cells  
528 showed an increase in quantum content [(as reported previously in rats (Sola et al., 2004)], IB2 KO  
529 granule cells showed an increased quantum size.

530 In aggregate, these results confirm that LTP in wild type mice depends almost exclusively  
531 on increased neurotransmitter release probability ( $>p$ ) and suggest that LTP in IB2 KO mice rests  
532 on a more complex mechanism including both changes in quantum content ( $>p$ ,  $n$ ) and quantum  
533 size ( $>q$ ).

534



535

536

**Figure 7. Mechanisms of LTP expression.**

537

(A) EPSC<sub>AMPA</sub> in WT and IB2 KO granule cells (average of 100 tracings in both cases) recorded in control and 20 min after HFS using paired-pulse stimulation (interstimulus interval 20 ms). The histogram shows the CV, PPR and EPSC<sub>AMPA</sub> amplitude changes following HFS in WT and IB2 KO mice. Data are reported as mean ± SEM; \*p<0.0, \*\*p<0.01.

540

(B) The  $(CV_2/CV_1)^2$  vs. (EPSC<sub>2</sub>/EPSC<sub>1</sub>) plot shows that WT LTP points fall in the sector of increased quantal release (>p,n) while IB2 KO points fall on the diagonal (>n) and in the sector of increased quantum size (>q).

541

(C) The traces show spontaneous synaptic activity before and after LTP induction in WT and IB2 KO granule cells. Following LTP induction, mEPSC frequency, but not amplitude, increased in WT while mEPSC amplitude, but not frequency, increased in IB2 KO mice.

542

(D) Examples of individual mEPSCs before and after LTP induction in WT and IB2 KO granule cells. The histograms compare changes in mEPSC frequency and amplitude during LTP in WT and IB2 KO mice. Data are reported as mean ± SEM; \*p<0.05.

543

[Source\\_Figure7](#)

544

545

546

547

548

549

550

**Altered spatial distribution of LTP and LTD in the granular layer of IB2 KO mice**

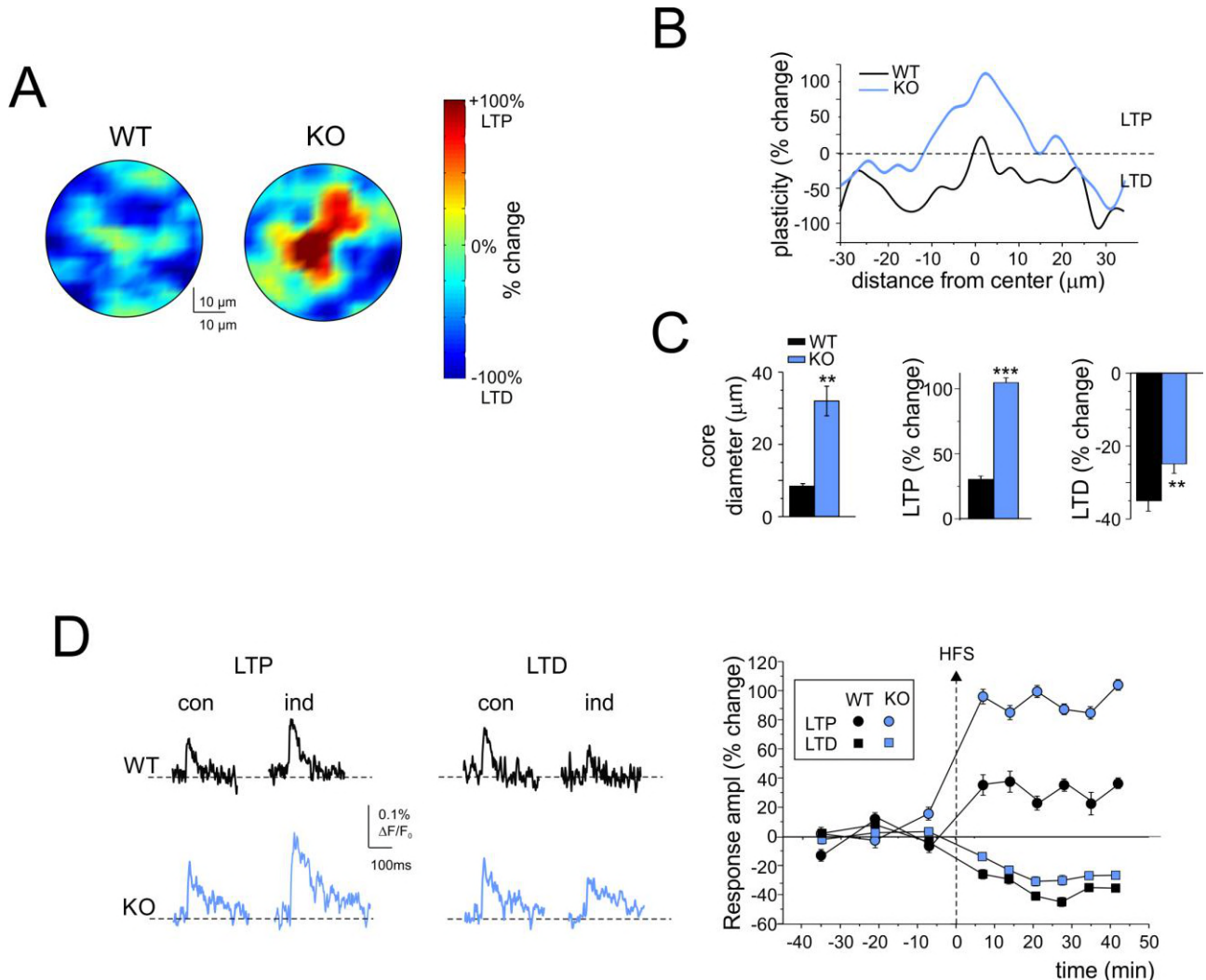
551

Given the enhanced LTP magnitude (cf. Fig. 5) and the altered C/S organization in IB2 KO granular layer (cf. Fig. 3), VSDi experiments were conducted in order to unravel possible alterations in the spatial distribution of LTP and LTD in IB2 KO granular layer. As recently shown using the same technique, the spatial distribution of areas undergoing LTP and LTD in the cerebellar granular layer displays a C/S-like organization, with LTP in the core and LTD in the surround (Gandolfi et al., 2015). The investigation of this feature in WT granular layer revealed a similar organization. Interestingly, the C/S organization of core-LTP and surround-LTD in IB2 KO granular layers showed a shape alteration with larger LTP cores and thinner LTD surrounds (Fig.8). The analysis of the granular layer areas with LTP and LTD revealed several abnormalities with respect to WT: i) LTP magnitude in the center was higher (WT = 28.4 ± 3.3% vs. IB2 KO = 109.4±6.7%, n=6 for both, p=8x10<sup>-6</sup>); ii) LTP total area underwent an impressive increase (WT = 3.3 ± 1.5% vs. IB2 KO = 10.2 ± 3.3%, n=6 for both; p=0.047), iii) LTD total area and magnitude were decreased (WT = 91.4±1.9% vs. IB2 KO = 81.3±3.7%, n=6 for both; p=0.037; total LTD magnitude: WT = -34.9±2.8% vs. IB2 KO = -24.9±2.6%, n=6 for both, p=0.0026), and iv) the C/S

564



565 shape showed a significant change in favor of LTP. In particular, the LTP-center was broader in IB2  
 566 KO compared to WT (core diameter: WT =  $8.4 \pm 0.7 \mu\text{m}$  vs. IB2 KO =  $32.0 \pm 4.1 \mu\text{m}$ , n=6  
 567 respectively; p=0.0005), and the LTD in the surround was less deep (WT =  $-37.3 \pm 1.5\%$  vs. IB2 KO  
 568 =  $-22.0 \pm 2.5\%$ ; n=6 for both; p=0.0004) (Fig. 8C,D).  
 569



570  
 571 **Figure 8. Spatial distribution of long-term plasticity of granular layer responses to mossy fiber stimulation.**  
 572 (A) VSDi normalized maps showing the spatial distribution of LTP and LTD in WT and IB2 KO granular layers (average of 6  
 573 recordings in both cases).  
 574 (B) The plot shows plasticity as a function of distance from the center for the maps shown in A. Note that in IB2 KO the LTP  
 575 magnitude in the core is larger, and that the core is broader than in WT.  
 576 (C) The histograms show, in WT and IB2 KO mice, the average core diameter and the LTP and LTD amplitude 30 minutes after HFS  
 577 (n=6 for both). Note that the IB2 KO granular layer shows larger LTP smaller LTD and larger cores than WT. Data are reported as  
 578 mean  $\pm$  SEM; \*\*\*p<0.001; \*\*p<0.01.  
 579 (D) VSDi recordings showing LTP and LTD of granular layer responses to mossy fiber stimulation. Exemplar traces before and 30  
 580 minutes after the induction protocol are reported for WT and IB2 KO. The plot shows the average time course of LTP and LTD for  
 581 WT and IB2 KO (n=6 for both). Data are reported as mean  $\pm$  SEM.

582 [Source\\_Figure8](#)

583  
 584  
 585  
 586  
 587

588

589

590

## Discussion

591

592

593

594

595

596

597

598

### ***Granule cell hyper-functioning and the NMDA receptor-dependent current***

599

600

601

602

603

604

605

606

607

608

609

610

611

612

613

In IB2 KO mice, cerebellar granule cells were hyper-functioning. *Enhanced synaptic transmission* appeared as a 2.4 times larger spike emission in response to high-frequency input bursts and was clearly correlated with larger NMDA receptor-mediated currents and increased intrinsic excitability. *Enhanced intrinsic excitability* appeared as a 2.1-7.1 (depending on current injection) higher efficiency in generating spikes during current injection and was correlated with larger Na<sup>+</sup> and K<sup>+</sup> membrane currents. *Enhanced synaptic plasticity* was manifest as a 5.3 times larger LTP compared to that normally measured at the mossy fiber - granule cell synapse (Prestori et al., 2008; Prestori et al., 2013). While normal LTP is almost entirely sustained by increased neurotransmitter release probability (Sola et al., 2004; D'Errico et al., 2009), IB2 KO LTP was expressed through a compound pre- and postsynaptic mechanism. This was consistently indicated by the increase in minis amplitude ( $>q$ ) and decrease in EPSC PPR ( $>n, p$ ) and confirmed by the ubiquitous distribution of points in the  $(CV_2/CV_1)^{-2}$  vs.  $(M_2/M_1)$  plot. The intervention of a postsynaptic expression mechanism was key to explain the neurotransmission increase in IB2 KO mice granule cells (~120%), which exceeds the theoretical limit of presynaptic expression alone (~60%; from (Sola et al., 2004)).

614

615

616

617

618

619

620

621

622

623

624

625

Interestingly, the whole set of alterations was likely to reflect, directly or indirectly, the NMDA receptor-mediated current enhancement occurring at the mossy fiber – granule cell synapse. In IB2 KO mice, the NMDA synaptic current of granule cells was increased by about 2.5 times, as anticipated by (Giza et al., 2010), while the AMPA receptor-mediated current was unaltered. During bursts, the granule cell NMDA current is known to exert a strong depolarizing action entraining a regenerative cycle (D'Angelo et al., 2005), in which depolarization removes NMDA channel unblock further increasing the NMDA current. The combination of this effect with enhanced intrinsic excitability could easily explain the enhanced synaptic transmission characterizing IB2 KO granule cells. In turn, enhanced NMDA receptor activation could also promote stronger plasticity of synaptic transmission and intrinsic excitability (Armano et al., 2000; Gall et al., 2005).

626

### ***Functional alterations of the granular layer microcircuit***

627

628

629

630

631

Given the absence of changes in synaptic inhibition, the enhancements in excitatory synaptic transmission and intrinsic excitability provide an explanation for the remarkable increase in E/I balance, for the prevalence of core over surround in C/S responses and for the extension of the LTP territory. The C/S organization of the cerebellum granular layer depends on the balance between granule cell excitation and Golgi cell inhibition (Mapelli and D'Angelo, 2007). Here, the strong

632 enhancement of the NMDA current could effectively counteract inhibition (Nieus et al., 2014)  
633 extending the core and changing the C/S from "Mexican hat" to "stovepipe hat" shape. The elevated  
634 input resistance and intrinsic excitability of IB2 KO granule cells could collaborate with elevated  
635 NMDA receptor-dependent transmission to spatially expand the excitatory footprint and zone of  
636 LTP. The consequences of NMDA receptor hyperfunctioning on the E/I balance and C/S changes  
637 could be further analyzed using realistic mathematical models of the granular layer (Solinas et al.,  
638 2010; Sudhakar et al., 2017).

639 NMDA receptor expression in granule cells is the strongest of cerebellum (Monaghan and  
640 Cotman, 1985) and is reasonable to speculate that a there damage could have a high impact on ASD  
641 pathogenesis. Although granular layer circuit alterations were uncompensated leading to a net E/I  
642 increase, some changes downstream might have a compensatory meaning. For example, in IB2 KO  
643 mice, the thinner molecular layer, the simplified dendritic tree and the smaller climbing fiber  
644 responses of Purkinje cells (Giza et al., 2010), may tend to limit the impact of granular layer  
645 overexcitation.

#### 646 647 ***Comparison of alterations with other circuits and ASD models***

648 The alterations observed in the cerebellum granular layer of IB2 KO mice resemble in some  
649 respects those observed in other brain structures of ASD mice. An enhanced NMDA receptor-  
650 mediated neurotransmission was proposed to cause hyper-reactivity and hyper-plasticity in the  
651 somatosensory cortex (Rinaldi et al., 2007; Rinaldi et al., 2008b), in pyramidal neurons of the  
652 medium prefrontal cortex (Rinaldi et al., 2008c) and in the amygdala (Markram et al., 2008).  
653 Interestingly, hyper-reactivity and hyper-plasticity were correlated with enhanced E/I balance in  
654 relation with enhanced NMDA receptor-mediated neurotransmission (Markram et al., 2008).  
655 Therefore, our results support the concept that enhanced NMDA receptor-mediated  
656 neurotransmission is a common bottleneck for ASD pathogenesis in different brain areas, including  
657 the cerebellum. The change of C/S shape from "Mexican hat" to "stovepipe hat" is especially  
658 interesting in view of the ASD hypothesis developed for cortical minicolumns, the fundamental  
659 module of the neocortex (Casanova et al., 2002; Casanova et al., 2006; Hutsler and Casanova,  
660 2016). The histological analysis postmortem of minicolumns in ASD patients has revealed reduced  
661 size and altered neuronal organization suggesting that lateral inhibition was reduced. In the C/S of  
662 the cerebellum granular layer, the *effectiveness* of lateral inhibition was indeed reduced by the  
663 increased intensity and extension of the excitation core. Therefore, a reduced effectiveness of  
664 surround inhibition of cortical and cerebellar modules may be a common trait of the disease in  
665 different brain microcircuits. The picture may be complicated by the interaction between causative,  
666 compensatory and developmental factors. For example, in *Gabrb3* mutants, an increased  
667 metabotropic glutamate receptor activation in deep cerebellar nuclei has been proposed to prevent  
668 the downstream propagation of effects and to protect from ASD in males (Mercer et al., 2016).

#### 669 670 ***Possible consequences of alterations on cerebellar functioning***

671 The cerebellar granular layer has been proposed to perform *expansion recoding* and *spatial*  
672 *pattern separation* of input signals (Marr, 1969), which can be regulated by long-term synaptic  
673 plasticity at the mossy fiber - granule cell relay (Hansel et al., 2001; D'Angelo and De Zeeuw, 2009;  
674 D'Angelo, 2014). In IB2 KO mice, mossy fiber burst retransmission was enhanced and the effect  
675 could be further amplified by LTP (Nieus et al., 2006). Moreover, the excited areas were broader

676 and poorly limited by surround inhibition. Therefore, expansion recoding and spatial pattern  
677 separation were likely to be compromised causing over-excitation of Purkinje cells and subsequent  
678 suppression of activity in deep-cerebellar nuclei. Altogether, these alterations could reverberate  
679 both on motor control (e.g. causing cerebellar motor symptoms) and on executive control (e.g.  
680 preventing novelty detection and attention switching) (D'Angelo and Casali, 2013), contributing to  
681 generate the combination of cerebellar and ASD symptoms presented by IB2 KO mice.

682

### 683 **Conclusions**

684 The complex derangement of signal processing and plasticity in the cerebellum granular  
685 layer of IB2 KO mice supports a causative role of cerebellum in ASD pathogenesis. Microcircuit  
686 alterations resembled the *hallmarks* reported for cortical minicolumns, including synaptic hyper-  
687 reactivity, synaptic hyper-plasticity, increased E/I balance and C/S changes. In the cerebellum, these  
688 alterations have the potential of contributing to ASD as well as motor symptoms. Executive control  
689 may be affected by a dysfunction of loops connecting the cerebellum to associative (especially  
690 prefrontal) areas (Palesi et al., 2017), impairing novelty detection and attention switching and  
691 contributing to generate ASD symptoms (Schmahmann, 2004; Schmahmann et al., 2007;  
692 Schmahmann, 2010; D'Angelo and Casali, 2013). Future challenges will be to determine how  
693 cerebellar alterations combine and co-evolve with those occurring in other brain regions (Bolduc  
694 and Limperopoulos, 2009; Limperopoulos et al., 2009; Bolduc et al., 2011; Wang et al., 2014;  
695 Hampson and Blatt, 2015; Mosconi et al., 2015) and contribute to determine the different  
696 syndromic forms of ASD (Broussard, 2014; Hampson and Blatt, 2015; Mosconi et al., 2015;  
697 Zeidán-Chuliá et al., 2016).

698

699

700

701  
702  
703  
704  
705  
706  
707  
708  
709  
710  
711  
712  
713  
714  
715  
716  
717  
718  
719  
720  
721  
722  
723  
724  
725  
726  
727  
728  
729  
730  
731  
732  
733  
734  
735  
736  
737  
738  
739  
740  
741  
742  
743  
744  
745  
746  
747  
748  
749  
750  
751  
752

## References

- Allen G (2006) Cerebellar contributions to autism spectrum disorders. *Clinical Neuroscience Research* 6:195-207.
- Amaral DG (2011) The promise and the pitfalls of autism research: an introductory note for new autism researchers. *Brain Res* 1380:3-9.
- Armano S, Rossi P, Taglietti V, D'Angelo E (2000) Long-term potentiation of intrinsic excitability at the mossy fiber-granule cell synapse of rat cerebellum. *J Neurosci* 20:5208-5216.
- Banerjee S, Riordan M, Bhat MA (2014) Genetic aspects of autism spectrum disorders: insights from animal models. *Front Cell Neurosci* 8:58.
- Bardoni R, Belluzzi O (1994) Modifications of A-current kinetics in mammalian central neurones induced by extracellular zinc. *J Physiol* 479 ( Pt 3):389-400.
- Bekkers JM, Stevens CF (1990) Presynaptic mechanism for long-term potentiation in the hippocampus. *Nature* 346:724-729.
- Betancur C (2011) Etiological heterogeneity in autism spectrum disorders: more than 100 genetic and genomic disorders and still counting. *Brain Res* 1380:42-77.
- Bolduc ME, Limperopoulos C (2009) Neurodevelopmental outcomes in children with cerebellar malformations: a systematic review. *Dev Med Child Neurol* 51:256-267.
- Bolduc ME, Du Plessis AJ, Sullivan N, Khwaja OS, Zhang X, Barnes K, Robertson RL, Limperopoulos C (2011) Spectrum of neurodevelopmental disabilities in children with cerebellar malformations. *Dev Med Child Neurol* 53:409-416.
- Brickley SG, Cull-Candy SG, Farrant M (1996) Development of a tonic form of synaptic inhibition in rat cerebellar granule cells resulting from persistent activation of GABAA receptors. *J Physiol* 497 ( Pt 3):753-759.
- Broussard DM (2014) *The Cerebellum: Learning Movement, Language, and Social Skills*. Clichester: John Wiley & Sons, Inc.
- Casanova MF (2003) Modular concepts of brain organization and the neuropathology of psychiatric conditions. *Psychiatry Res* 118:101-102.
- Casanova MF (2006) Neuropathological and genetic findings in autism: the significance of a putative minicolumnopathy. *Neuroscientist* 12:435-441.
- Casanova MF, Buxhoeveden DP, Brown C (2002) Clinical and macroscopic correlates of minicolumnar pathology in autism. *J Child Neurol* 17:692-695.
- Casanova MF, van Kooten IA, Switala AE, van Engeland H, Heinsen H, Steinbusch HW, Hof PR, Trippe J, Stone J, Schmitz C (2006) Minicolumnar abnormalities in autism. *Acta Neuropathol* 112:287-303.
- Cathala L, Brickley S, Cull-Candy S, Farrant M (2003) Maturation of EPSCs and intrinsic membrane properties enhances precision at a cerebellar synapse. In: *J Neurosci*, pp 6074-6085. United States.
- Cesana E, Pietrajtis K, Bidoret C, Isope P, D'Angelo E, Dieudonné S, Forti L (2013) Granule cell ascending axon excitatory synapses onto Golgi cells implement a potent feedback circuit in the cerebellar granular layer. *J Neurosci* 33:12430-12446.
- Courchesne E, Allen G (1997) Prediction and preparation, fundamental functions of the cerebellum. *Learn Mem* 4:1-35.
- Curatolo P, Ben-Ari Y, Bozzi Y, Catania MV, D'Angelo E, Mapelli L, Oberman LM, Rosenmund C, Cherubini E (2014) Synapses as therapeutic targets for autism spectrum disorders: an international symposium held in pavia on July 4th, 2014. *Front Cell Neurosci* 8:309.
- D'Angelo E (2014) The organization of plasticity in the cerebellar cortex: from synapses to control. *Prog Brain Res* 210:31-58.
- D'Angelo E, De Zeeuw CI (2009) Timing and plasticity in the cerebellum: focus on the granular layer. *Trends Neurosci* 32:30-40.
- D'Angelo E, Casali S (2013) Seeking a unified framework for cerebellar function and dysfunction: from circuit operations to cognition. *Frontiers in Neural Circuits* 6.
- D'Angelo E, De Filippi G, Rossi P, Taglietti V (1995) Synaptic excitation of individual rat cerebellar granule cells in situ: evidence for the role of NMDA receptors. *J Physiol* 484 ( Pt 2):397-413.

- 753 D'Angelo E, De Filippi G, Rossi P, Taglietti V (1998) Ionic mechanism of electroresponsiveness in cerebellar  
754 granule cells implicates the action of a persistent sodium current. *J Neurophysiol* 80:493-503.
- 755 D'Angelo E, Rossi P, Armano S, Taglietti V (1999) Evidence for NMDA and mGlu receptor-dependent long-  
756 term potentiation of mossy fiber-granule cell transmission in rat cerebellum. *J Neurophysiol*  
757 81:277-287.
- 758 D'Angelo E, Rossi P, Gall D, Prestori F, Nieuwenhuis T, Maffei A, Sola E (2005) Long-term potentiation of synaptic  
759 transmission at the mossy fiber-granule cell relay of cerebellum. *Prog Brain Res* 148:69-80.
- 760 D'Errico A, Prestori F, D'Angelo E (2009) Differential induction of bidirectional long-term changes in  
761 neurotransmitter release by frequency-coded patterns at the cerebellar input. *J Physiol* 587:5843-  
762 5857.
- 763 De Rubeis S, Buxbaum JD (2015) Genetics and genomics of autism spectrum disorder: embracing  
764 complexity. *Hum Mol Genet* 24:R24-31.
- 765 Ellegood J et al. (2015) Clustering autism: using neuroanatomical differences in 26 mouse models to gain  
766 insight into the heterogeneity. *Mol Psychiatry* 20:118-125.
- 767 Gall D, Prestori F, Sola E, D'Errico A, Roussel C, Forti L, Rossi P, D'Angelo E (2005) Intracellular calcium  
768 regulation by burst discharge determines bidirectional long-term synaptic plasticity at the  
769 cerebellum input stage. *J Neurosci* 25:4813-4822.
- 770 Gandolfi D, Mapelli J, D'Angelo E (2015) Long-Term Spatiotemporal Reconfiguration of Neuronal Activity  
771 Revealed by Voltage-Sensitive Dye Imaging in the Cerebellar Granular Layer. *Neural Plast*  
772 2015:284986.
- 773 Gandolfi D, Pozzi P, Tognolina M, Chirico G, Mapelli J, D'Angelo E (2014) The spatiotemporal organization of  
774 cerebellar network activity resolved by two-photon imaging of multiple single neurons. *Front Cell*  
775 *Neurosci* 8:92.
- 776 Giza J, Urbanski MJ, Prestori F, Bandyopadhyay B, Yam A, Friedrich V, Kelley K, D'Angelo E, Goldfarb M  
777 (2010) Behavioral and cerebellar transmission deficits in mice lacking the autism-linked gene *islet*  
778 *brain-2*. *J Neurosci* 30:14805-14816.
- 779 Gogolla N, Leblanc JJ, Quast KB, Südhof TC, Fagiolini M, Hensch TK (2009) Common circuit defect of  
780 excitatory-inhibitory balance in mouse models of autism. *J Neurodev Disord* 1:172-181.
- 781 Hampson DR, Blatt GJ (2015) Autism spectrum disorders and neuropathology of the cerebellum. *Front*  
782 *Neurosci* 9:420.
- 783 Hansel C, Linden DJ, D'Angelo E (2001) Beyond parallel fiber LTD: the diversity of synaptic and non-synaptic  
784 plasticity in the cerebellum. *Nat Neurosci* 4:467-475.
- 785 Hutsler JJ, Casanova MF (2016) Review: Cortical construction in autism spectrum disorder: columns,  
786 connectivity and the subplate. *Neuropathol Appl Neurobiol* 42:115-134.
- 787 Ito M (2008) Control of mental activities by internal models in the cerebellum. *Nat Rev Neurosci* 9:304-313.
- 788 Kim H, Lim CS, Kaang BK (2016) Neuronal mechanisms and circuits underlying repetitive behaviors in mouse  
789 models of autism spectrum disorder. *Behav Brain Funct* 12:3.
- 790 Kloth AD, Badura A, Li A, Cherskov A, Connolly SG, Giovannucci A, Bangash MA, Grasselli G, Peñagarikano O,  
791 Piochon C, Tsai PT, Geschwind DH, Hansel C, Sahin M, Takumi T, Worley PF, Wang SS (2015)  
792 Cerebellar associative sensory learning defects in five mouse autism models. *Elife* 4:e06085.
- 793 Kullmann DM, Nicoll RA (1992) Long-term potentiation is associated with increases in quantal content and  
794 quantal amplitude. *Nature* 357:240-244.
- 795 Limperopoulos C, Robertson RL, Sullivan NR, Bassan H, du Plessis AJ (2009) Cerebellar injury in term infants:  
796 clinical characteristics, magnetic resonance imaging findings, and outcome. *Pediatr Neurol* 41:1-8.
- 797 Maffei A, Prestori F, Shibuki K, Rossi P, Taglietti V, D'Angelo E (2003) NO enhances presynaptic currents  
798 during cerebellar mossy fiber-granule cell LTP. *J Neurophysiol* 90:2478-2483.
- 799 Magistretti J, Castelli L, Forti L, D'Angelo E (2006) Kinetic and functional analysis of transient, persistent and  
800 resurgent sodium currents in rat cerebellar granule cells in situ: an electrophysiological and  
801 modelling study. *J Physiol* 573:83-106.
- 802 Malgaroli A, Ting AE, Wendland B, Bergamaschi A, Villa A, Tsien RW, Scheller RH (1995) Presynaptic  
803 component of long-term potentiation visualized at individual hippocampal synapses. *Science*  
804 268:1624-1628.

- 805 Malinow R, Tsien RW (1990) Presynaptic enhancement shown by whole-cell recordings of long-term  
806 potentiation in hippocampal slices. *Nature* 346:177-180.
- 807 Manabe T, Wyllie DJ, Perkel DJ, Nicoll RA (1993) Modulation of synaptic transmission and long-term  
808 potentiation: effects on paired pulse facilitation and EPSC variance in the CA1 region of the  
809 hippocampus. *J Neurophysiol* 70:1451-1459.
- 810 Mapelli J, D'Angelo E (2007) The spatial organization of long-term synaptic plasticity at the input stage of  
811 cerebellum. *J Neurosci* 27:1285-1296.
- 812 Mapelli J, Gandolfi D, D'Angelo E (2010) Combinatorial responses controlled by synaptic inhibition in the  
813 cerebellum granular layer. *J Neurophysiol* 103:250-261.
- 814 Mapelli L, Solinas S, D'Angelo E (2014) Integration and regulation of glomerular inhibition in the cerebellar  
815 granular layer circuit. *Front Cell Neurosci* 8:55.
- 816 Mapelli L, Rossi P, Nieuwenhuis T, D'Angelo E (2009) Tonic activation of GABAB receptors reduces release  
817 probability at inhibitory connections in the cerebellar glomerulus. *J Neurophysiol* 101:3089-3099.
- 818 Markram K, Markram H (2010) The intense world theory - a unifying theory of the neurobiology of autism.  
819 *Front Hum Neurosci* 4:224.
- 820 Markram K, Rinaldi T, La Mendola D, Sandi C, Markram H (2008) Abnormal fear conditioning and amygdala  
821 processing in an animal model of autism. *Neuropsychopharmacology* 33:901-912.
- 822 Marr D (1969) A theory of cerebellar cortex. *J Physiol* 202:437-470.
- 823 Mercer AA, Palarz KJ, Tabatadze N, Woolley CS, Raman IM (2016) Sex differences in cerebellar synaptic  
824 transmission and sex-specific responses to autism-linked Gabrb3 mutations in mice. *Elife* 5.
- 825 Monaghan DT, Cotman CW (1985) Distribution of N-methyl-D-aspartate-sensitive L-[3H]glutamate-binding  
826 sites in rat brain. *J Neurosci* 5:2909-2919.
- 827 Mosconi MW, Wang Z, Schmitt LM, Tsai P, Sweeney JA (2015) The role of cerebellar circuitry alterations in  
828 the pathophysiology of autism spectrum disorders. *Front Neurosci* 9:296.
- 829 Nieuwenhuis T, Sola E, Mapelli J, Saftenku E, Rossi P, D'Angelo E (2006) LTP regulates burst initiation and frequency  
830 at mossy fiber-granule cell synapses of rat cerebellum: experimental observations and theoretical  
831 predictions. *J Neurophysiol* 95:686-699.
- 832 Nieuwenhuis TR, Mapelli L, D'Angelo E (2014) Regulation of output spike patterns by phasic inhibition in cerebellar  
833 granule cells. *Front Cell Neurosci* 8:246.
- 834 Palesi F, De Rinaldis A, Castellazzi G, Calamante F, Muhlert N, Chard D, Tournier JD, Magenes G, D'Angelo E,  
835 Gandini Wheeler-Kingshott CAM (2017) Contralateral cortico-ponto-cerebellar pathways  
836 reconstruction in humans in vivo: implications for reciprocal cerebro-cerebellar structural  
837 connectivity in motor and non-motor areas. *Sci Rep* 7:12841.
- 838 Prestori F, Rossi P, Bearzatto B, Lainé J, Necchi D, Diwakar S, Schiffmann S, Axelrad H, D'Angelo E (2008)  
839 Altered neuron excitability and synaptic plasticity in the cerebellar granular layer of juvenile prion  
840 protein knock-out mice with impaired motor control. *J Neurosci* 28:7091-7103.
- 841 Prestori F, Bonardi C, Mapelli L, Lombardo P, Goselink R, De Stefano ME, Gandolfi D, Mapelli J, Bertrand D,  
842 Schonewille M, De Zeeuw C, D'Angelo E (2013) Gating of long-term potentiation by nicotinic  
843 acetylcholine receptors at the cerebellum input stage. *PLoS One* 8:e64828.
- 844 Qiu S, Aldinger KA, Levitt P (2012) Modeling of autism genetic variations in mice: focusing on synaptic and  
845 microcircuit dysfunctions. *Dev Neurosci* 34:88-100.
- 846 Rinaldi T, Perrodin C, Markram H (2008a) Hyper-connectivity and hyper-plasticity in the medial prefrontal  
847 cortex in the valproic Acid animal model of autism. *Front Neural Circuits* 2:4.
- 848 Rinaldi T, Silberberg G, Markram H (2008b) Hyperconnectivity of local neocortical microcircuitry induced by  
849 prenatal exposure to valproic acid. *Cereb Cortex* 18:763-770.
- 850 Rinaldi T, Perrodin C, Markram H (2008c) Hyper-connectivity and hyper-plasticity in the medial prefrontal  
851 cortex in the valproic Acid animal model of autism. *Front Neural Circuits* 2:4.
- 852 Rinaldi T, Kulangara K, Antonello K, Markram H (2007) Elevated NMDA receptor levels and enhanced  
853 postsynaptic long-term potentiation induced by prenatal exposure to valproic acid. *Proc Natl Acad Sci U S A* 104:13501-13506.
- 854

- 855 Rossi P, De Filippi G, Armano S, Taglietti V, D'Angelo E (1998) The weaver mutation causes a loss of inward  
856 rectifier current regulation in premigratory granule cells of the mouse cerebellum. *J Neurosci*  
857 18:3537-3547.
- 858 Rubenstein JL, Merzenich MM (2003) Model of autism: increased ratio of excitation/inhibition in key neural  
859 systems. *Genes Brain Behav* 2:255-267.
- 860 Saviane C, Silver RA (2006) Errors in the estimation of the variance: implications for multiple-probability  
861 fluctuation analysis. *J Neurosci Methods* 153:250-260.
- 862 Schmahmann JD (2004) Disorders of the cerebellum: ataxia, dysmetria of thought, and the cerebellar  
863 cognitive affective syndrome. *J Neuropsychiatry Clin Neurosci* 16:367-378.
- 864 Schmahmann JD (2010) The role of the cerebellum in cognition and emotion: personal reflections since  
865 1982 on the dysmetria of thought hypothesis, and its historical evolution from theory to therapy.  
866 *Neuropsychol Rev* 20:236-260.
- 867 Schmahmann JD, Weilburg JB, Sherman JC (2007) The neuropsychiatry of the cerebellum - insights from the  
868 clinic. *Cerebellum* 6:254-267.
- 869 Sgritta M, Locatelli F, Soda T, Prestori F, D'Angelo EU (2017) Hebbian Spike-Timing Dependent Plasticity at  
870 the Cerebellar Input Stage. *J Neurosci* 37:2809-2823.
- 871 Sharma G, Vijayaraghavan S (2003) Modulation of presynaptic store calcium induces release of glutamate  
872 and postsynaptic firing. In: *Neuron*, pp 929-939. United States.
- 873 Silver RA, Cull-Candy SG, Takahashi T (1996) Non-NMDA glutamate receptor occupancy and open  
874 probability at a rat cerebellar synapse with single and multiple release sites. *J Physiol* 494 ( Pt  
875 1):231-250.
- 876 Sola E, Prestori F, Rossi P, Taglietti V, D'Angelo E (2004) Increased neurotransmitter release during long-  
877 term potentiation at mossy fibre-granule cell synapses in rat cerebellum. *J Physiol* 557:843-861.
- 878 Solinas S, Nieuwenhuis T, D'Angelo E (2010) A realistic large-scale model of the cerebellum granular layer predicts  
879 circuit spatio-temporal filtering properties. *Front Cell Neurosci* 4:12.
- 880 Sudhakar SK, Hong S, Raikov I, Publio R, Lang C, Close T, Guo D, Negrello M, De Schutter E (2017)  
881 Spatiotemporal network coding of physiological mossy fiber inputs by the cerebellar granular layer.  
882 *PLoS Comput Biol* 13:e1005754.
- 883 Sztainberg Y, Zoghbi HY (2016) Lessons learned from studying syndromic autism spectrum disorders. *Nat*  
884 *Neurosci* 19:1408-1417.
- 885 Tsai PT (2016) Autism and cerebellar dysfunction: Evidence from animal models. *Semin Fetal Neonatal*  
886 *Med*.
- 887 Tu S et al. (2017) NitroSynapsin therapy for a mouse MEF2C haploinsufficiency model of human autism. *Nat*  
888 *Commun* 8:1488.
- 889 Uzunova G, Pallanti S, Hollander E (2015) Excitatory/inhibitory imbalance in autism spectrum disorders:  
890 Implications for interventions and therapeutics. *World J Biol Psychiatry*:1-13.
- 891 Vranesic I, Iijima T, Ichikawa M, Matsumoto G, Knöpfel T (1994) Signal transmission in the parallel fiber-  
892 Purkinje cell system visualized by high-resolution imaging. *Proc Natl Acad Sci U S A* 91:13014-  
893 13017.
- 894 Wang SS, Kloth AD, Badura A (2014) The cerebellum, sensitive periods, and autism. *Neuron* 83:518-532.
- 895 Wyllie DJ, Manabe T, Nicoll RA (1994) A rise in postsynaptic Ca<sup>2+</sup> potentiates miniature excitatory  
896 postsynaptic currents and AMPA responses in hippocampal neurons. *Neuron* 12:127-138.
- 897 Yang Y, Calakos N (2013) Presynaptic long-term plasticity. *Front Synaptic Neurosci* 5:8.
- 898 Yasuda J, Whitmarsh AJ, Cavanagh J, Sharma M, Davis RJ (1999) The JIP group of mitogen-activated protein  
899 kinase scaffold proteins. *Mol Cell Biol* 19:7245-7254.
- 900 Zeidán-Chuliá F, de Oliveira BH, Casanova MF, Casanova EL, Noda M, Salmina AB, Verkhratsky A (2016) Up-  
901 Regulation of Oligodendrocyte Lineage Markers in the Cerebellum of Autistic Patients: Evidence  
902 from Network Analysis of Gene Expression. *Mol Neurobiol* 53:4019-4025.
- 903 Zucker RS, Regehr WG (2002) Short-term synaptic plasticity. *Annu Rev Physiol* 64:355-405.

904